

# Lunar Electrical Conductivity, Permeability, and Temperature from Apollo Magnetometer Experiments

P. Dyal

*NASA/Ames Research Center  
Moffett Field, California*

C. W. Parkin

*University of Santa Clara  
Santa Clara, California*

W. D. Daily

*Brigham Young University  
Provo, Utah*

Magnetometers have been deployed at four Apollo sites on the Moon to measure remanent and induced lunar magnetic fields. Measurements from this network of instruments have been used to calculate the electrical conductivity, temperature, magnetic permeability, and iron abundance of the lunar interior. The measured lunar remanent fields range from 3 gammas ( $\gamma$ ) minimum at the Apollo 15 site to 327  $\gamma$  maximum at the Apollo 16 site. Simultaneous magnetic field and solar plasma pressure measurements show that the remanent fields at the Apollo 12 and 16 sites interact with, and are compressed by, the solar wind. Remanent fields at Apollo 12 and Apollo 16 are increased 16  $\gamma$  and 32  $\gamma$ , respectively, by a solar plasma bulk pressure increase of  $1.5 \times 10^{-7}$  dynes/cm<sup>2</sup>. Global lunar fields due to eddy currents, induced in the lunar interior by magnetic transients, have been analyzed to calculate an electrical conductivity profile for the Moon. From nightside magnetometer data in the solar wind it has been found that deeper than 170 km into the Moon the conductivity rises from  $3 \times 10^{-4}$  mhos/m to  $10^{-2}$  mhos/m at 1000-km depth. Recent analysis of data obtained in the geomagnetic tail, in regions free of complicating plasma effects, yields results consistent with nightside values. Conductivity profiles have been used to calculate the lunar temperature for an assumed lunar material of olivine. In the outer layer ( $\sim 170$  km thick) the temperature rises to 110° C, after which it gradually increases with depth to 1500° C at a depth of  $\sim 1000$  km. Simultaneous measurements by magnetometers on the lunar surface and in orbit around the moon are used to construct a whole-moon hysteresis curve, from which the global lunar magnetic permeability is determined to be  $\mu = 1.012 \pm 0.006$ . The corresponding global induced dipole moment is  $2 \times 10^{18}$  gauss-cm<sup>3</sup> for typical inducing fields of  $10^{-4}$  gauss in the lunar environment. Lunar free iron abundance corresponding to the global permeability is determined to be  $2.5 \pm 2.0$  wt. %. Total iron abundance (sum of iron in the ferromagnetic and paramagnetic states) is calculated for two assumed compositional models of the lunar interior. For a free iron/orthopyroxene lunar composition the total iron content is calculated to be  $12.8 \pm 1.0$  wt. %; for a free iron/olivine composition, total iron content is  $5.5 \pm 1.2$  wt. %. Other lunar models with an iron core and with a shallow iron-rich layer are also discussed in light of the measured global lunar permeability. Velocities and thicknesses of the Earth's magnetopause and bow shock have been estimated from simultaneous magnetometer measurements. Average speeds are determined to be about 50 km/s for the magnetopause and 70 km/s for the bow shock, although there are large variations in the measurement for any particular boundary crossing. Corresponding measured boundary thicknesses average about 2300 km for the magnetopause and 1400 km for the bow shock.

Magnetometers placed on the lunar surface and in orbit about the Moon have returned a wealth of information about the Moon which was not anticipated prior to the Apollo manned lunar missions. Earlier measurements, by U.S.S.R. and U.S. magnetometers on unmanned spacecraft, indicated that the Moon might be electromagnetically inert; during that time investigators often concentrated on the interactions of the Moon with the solar wind plasma (refs. 1-4) rather than on magnetic studies of the lunar interior. Studies of the lunar interior prior to the Apollo landings (e.g., see refs. 2 and 5-9) were constrained by the lack of high resolution measurements of whole body induction fields near the Moon.

The measurement of magnetic fields in the vicinity of the Moon began in January 1959, when the U.S.S.R. spacecraft Luna 1 carried a magnetometer to within several hundred kilometers of the Moon. In September 1959, Luna 2, also equipped with a magnetometer, impacted the lunar surface. The instrument aboard Luna 2 set an upper limit of 100 gammas (1 gamma =  $10^{-5}$  gauss) for a possible lunar field at an altitude of about 50 km above the Moon's surface (ref. 10). In April 1966, Luna 10 carrying a magnetometer 10 times more sensitive than that aboard Luna 2, was successfully placed in a lunar orbit that came to within 350 km of the Moon. The Luna 10 magnetometer recorded a time-varying magnetic field in the vicinity of the Moon, which was at that time interpreted as indicating the existence of a weak lunar magnetosphere (ref. 11), although later studies modified this interpretation.

A year later (July 1967) the United States placed the Explorer 35 satellite, with two magnetometers aboard, in orbit around the Moon. In its orbit the satellite passed to within 830 km of the Moon's surface. Explorer 35 successfully measured magnetic properties of the solar-wind cavity downstream from the Moon, but it did not detect the lunar magnetosphere indicated by Luna 10 measurements nor the lunar bow shock and induced-field configuration previously

suggested by Gold (ref. 12). In an analysis of the Explorer 35 results, Sonett et. al. (ref. 13) concluded that if a permanent lunar field exists at all, its magnitude would be less than two gammas at an altitude of 830 km and therefore  $\leq 4$  gammas at the surface for a global permanent dipole field. The upper limit on the global permanent dipole moment was set at  $10^{20}$  gauss-cm<sup>3</sup>, i.e., less than  $10^{-5}$  that of the Earth. In studies of the solar wind interaction with the lunar body (refs. 1 and 2), investigators found the solar wind field magnitude to be  $\sim 1.5$  gammas greater in the diamagnetic cavity on the Moon's antisolar side than in the solar wind.

Surveyor spacecraft, used in the first U.S. unmanned lunar landings, carried no magnetometers. Permanent magnets were carried aboard the Surveyor 5 and 6 spacecraft, however, which demonstrated that soils at those two landing sites contain less than 1 percent (by volume) ferromagnetic iron (ref. 14).

During the early manned Apollo missions it was determined that the Moon is much more interesting magnetically than had been expected. Natural remanent magnetization in lunar samples was found to be surprisingly high at all U.S. Apollo sites and at the U.S.S.R. Luna 16 site (see, for example, refs. 15-21). Such high natural remanent magnetism implies that at some time in the past there existed an ambient surface magnetic field considerably higher than that which now exists on the Moon (refs. 16 and 22).

The first lunar surface magnetometer (LSM), deployed at the Apollo 12 site in November 1969, made the first direct measurement of an intrinsic lunar magnetic field (ref. 23). The 38-gamma field measurement showed that not only are individual rocks magnetized but also that magnetization in the lunar crust can be ordered over much larger regions of 2-km to 200-km scale sizes (refs. 23 and 24). The permanent and induced fields measured by the Apollo 12 magnetometer provided the impetus to develop portable surface magnetometers and satellite magnetometers for later Apollo missions. Permanent mag-

netic fields were subsequently measured at four other landing sites: Apollo 14 (103  $\gamma$  maximum), Apollo 15 (3  $\gamma$ ), Apollo 16 (327  $\gamma$  maximum), and more recently at several positions along the U.S.S.R. Lunokhod II traverse. The surface fields were attributed to local magnetized sources ("magcons"); their discovery prompted a reexamination of Explorer 35 magnetometer data by Mihalov et al. (ref. 25), who found indirect evidence that several magnetized regions exist in the lunar crust. Direct field measurements from Apollo 15 and 16 subsatellite magnetometers, activated in August 1971 and April 1972, respectively, yielded maps of some of the larger magnetized regions in the lunar crust (refs. 26 and 27) which confirmed the existence of magnetized regions over much of the lunar surface. Subsatellite magnetometer measurements have also placed an upper limit of  $4.4 \times 10^{13}$  gauss-cm<sup>3</sup> on the global permanent magnetic dipole moment (ref. 28).

Investigations of simultaneous surface magnetometer data and solar wind spectrometer data show that the surface remanent magnetic fields interact with the solar wind when on the dayside of the moon (refs. 29, 30, and 31). The interaction is interpreted as a compression of the surface remanent fields by the solar wind; the magnetic pressure at the surface increases in proportion to the dynamic bulk pressure of the solar wind plasma.

In addition to measuring permanent lunar fields, the network of lunar surface and orbiting magnetometers measured fields induced in the lunar interior by extralunar magnetic fields, allowing investigation of deep interior properties of the Moon. Behanon (ref. 8) placed an upper limit of 1.8 on the bulk relative magnetic permeability by studying Explorer 35 magnetometer measurements in the geomagnetic tail. Subsequently, simultaneous measurements of Explorer 35 and Apollo 12 magnetometers have been used to yield the more accurate value of  $1.012 \pm 0.006$  (refs. 32 and 33). Recent Apollo 15 subsatellite magnetometer measurements have indicated the existence of a possible lunar ionosphere, which could affect the whole-Moon permeability calculations (ref.

34); effects of a lunar ionosphere on iron abundance determinations are considered by Parkin et al. (ref. 32).

The electrical conductivity of the lunar interior has been investigated by analyzing the induction of global lunar fields by time-varying extralunar (solar or terrestrial) magnetic fields. Since temperature and conductivity of geological materials are related, calculated conductivity profiles have been used to infer temperature of the lunar interior. Early estimates of bulk lunar electrical conductivity were made from lunar-orbiting Explorer 35 data by Colburn et al. (ref. 1) and Ness (ref. 7). For homogeneous-conductivity models of the Moon, Colburn et al. placed an upper limit of  $10^{-6}$  mhos/m for whole-Moon conductivity, whereas Ness' upper limit was  $10^{-5}$  mhos/m. These investigators also stated that their measurements were consistent with a higher conductivity lunar core surrounded by an insulating crust.

Theoretical studies of the electrodynamic response of the Moon to time-dependent external fields have been undertaken by many authors. Two types of whole-Moon magnetic induction fields have been treated: a poloidal field due to eddy currents driven by time-varying external magnetic fields, and a toroidal field due to unipolar currents driven through the Moon by the motional solar-wind  $V \times B$  electric field.

The toroidal induction mode, first suggested to be an important process in the Moon by Sonett and Colburn (ref. 5), was later developed in detail theoretically for a lunar model totally confined by the highly conducting solar wind (refs. 35, 36, and 37). However, analysis of simultaneous Apollo 12 and Explorer 35 magnetometer data later indicated that for the Moon, toroidal induction is negligible in comparison to poloidal induction; upper limits on the toroidal field mode were used to calculate an upper limit of  $10^{-9}$  mhos/m for electrical conductivity of the outer 5 km of the lunar crust (ref. 38). In subsequent analysis of lunar electromagnetic induction, toroidal induction has been assumed to be negligible relative to poloidal induction.

The eddy-current response of a homogeneous sphere in a vacuum to time-varying magnetic fields has been described by Smythe (ref. 39) and Wait (ref. 40). Early theoretical application of vacuum poloidal induction to studies of the lunar interior were presented by Gold (ref. 12) and Tozer and Wilson (ref. 41). Poloidal response theory for a lunar sphere totally confined by a highly conducting plasma was developed by Blank and Sill (ref. 42), Schubert and Schwartz (ref. 36), and Sill and Blank (ref. 37).

Since deployment of the Apollo 12 magnetometer in November 1969, electrical conductivity analysis has been developed with two basic approaches: a time-dependent, transient-response technique (refs. 43, 44, and 45) and a frequency-dependent, Fourier-harmonic technique (refs. 44 and 46-49). Past analyses have all used magnetometer data recorded at times when global eddy-current fields were asymmetrically confined by the solar wind plasma (refs. 45 and 50-53). The asymmetric confinement of lunar fields is particularly complex to model theoretically (ref. 54); indeed, the general time-dependent asymmetric induction problem has not been solved at the time of this writing. To avoid these complications, recent conductivity analysis has used field data recorded in the geomagnetic tail, which is relatively free of plasma and asymmetric confinement effects. Preliminary results of this analysis will be presented in this paper.

The purpose of this paper is to review the application of lunar magnetic field measurements to the study of properties of the lunar crust and deep interior. Following a brief descriptive section on lunar magnetometers and the lunar magnetic environment, measurements of lunar remanent fields and their interaction with the solar plasma will be discussed. The magnetization induction mode will be considered with reference to lunar magnetic permeability and iron abundance calculations. Electrical conductivity and temperature calculations from analyses of poloidal induction, for data taken in both the solar wind and in the geomagnetic tail, will be reviewed. Finally, properties of

the Earth's magnetopause and bow shock measured by lunar magnetometers will be discussed.

## The Apollo Surface Magnetometers

### LUNAR SURFACE MAGNETOMETER (LSM)

Lunar surface magnetometers, designed to measure and transmit data continuously to Earth for at least one year, have been deployed at three sites on the moon: Apollo 12 (coordinates  $3.0^\circ$  south latitude,  $23.4^\circ$  west longitude), Apollo 15 ( $26.1^\circ$  N,  $3.7^\circ$  E), and Apollo 16 ( $9.0^\circ$  S,  $15.5^\circ$  E). A photograph of the LSM fully deployed and aligned at the Descartes landing site is shown in figure 1 and the Apollo 16 LSM characteristics are given in table 1. (A detailed description of this instrument is provided by Dyal et al., ref. 55).

### Mechanical and Thermal Subsystems

In the exterior mechanical and thermal configuration of the Apollo LSM, the three fluxgate sensors are located at the ends of three 100-cm-long orthogonal booms that separate the sensors from each other by 150 cm, and position them 75 cm above the lunar surface (fig. 2). Orientation measurements with respect to lunar coordinates are made with two devices. A shadowgraph and bubble level are used by the astronaut to align the LSM and to measure azimuthal orientation with respect to the Moon-to-Sun line to an accuracy of  $0.5^\circ$ . Gravity-level sensors measure instrument tilt angles to an accuracy of  $0.2^\circ$  every 4.8 seconds.

In addition to the instrument normal mode of operation in which three vector field components are measured, the LSM has a gradiometer mode in which commands are sent to operate three motors, which rotate the sensors such that all simultaneously align in a parallel manner, first to one of the three boom axes, then to each of the other two boom axes in



Figure 1.—The Apollo lunar surface magnetometer (LSM) deployed on the Moon at the Apollo 16 Descartes site. Magnetic field sensors are at the top ends of the booms and approximately 75 cm above the lunar surface.

Table 1.—*Apollo Surface Magnetometer Characteristics*

Parameter	Apollo 16 Stationary Magnetometer (LSM)	Apollo 16 Portable Magnetometer (LPM)
Ranges, Gammas (each sensor)	0 to $\pm 200$ 0 to $\pm 100$ 0 to $\pm 50$	0 to $\pm 256$
Resolution, Gammas	0.1	1.0
Frequency Response, Hz	dc to 3	dc to 0.05
Angular Response	Cosine of angle between field and sensor	Cosine of angle between field and sensor
Sensor Geometry	3 orthogonal sensors at ends of 100-cm booms	3 orthogonal sensors in 6-cm cube
Analog Zero Determination	180° flip of sensor	180° flip of sensor
Power, Watts	3.5	1.5 (battery)
Weight, kg	8.9	4.6
Size, cm	63 x 28 x 25	56 x 15 x 14
Operating Temperature, °C	-50 to +85	0 to +50
Commands	10 ground: 1 spacecraft	—

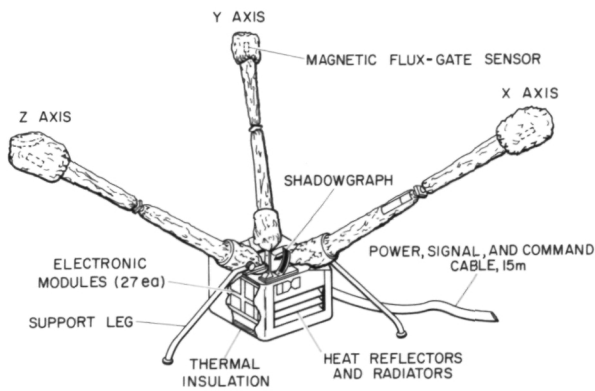


Figure 2.—Schematic diagram of the lunar surface magnetometer (LSM) without the sunshade shown in figure 1. Sensors are at the top ends of the booms and approximately 75 cm above the ground. The electronics and motor drive assembly are located in the box, encased in a thermal blanket. Heat rejection during lunar day and retention during lunar night are controlled by a parabolic reflector array on two sides of the electronics box. The astronaut bubble level and azimuthal shadowgraph are shown on top of the box. Power, digital signals, and commands are provided through the ribbon cable which connects to the central station telemetry receiver and transmitter.

turn. This rotating alignment permits the vector gradient to be calculated in the plane of the sensors, and also permits an independent measurement of the magnetic field vector at each sensor position.

The thermal subsystem is designed to allow the LSM to operate over the complete lunar day-night cycle. Thermal control is accomplished by a combination of insulation, control surfaces, and heaters that operate collectively to keep the electronics between 267 K and 319 K. A plot of the temperature of the X sensor and the electronics for the first post-deployment lunation is shown in figure 3 for the Apollo 16 LSM.

## Electronics

The electronic components for the LSM are located in the thermally insulated box. The operation of the electronics is illustrated in figure 4. Long-term stability is attained by extensive use of digital circuitry, by internal calibration of the analog portion of the instrument every 18 hours, and by mechanical rotation of each sensor through 180° to determine the sensor zero offset. The analog output of the sensor electronics is internally processed by a low-pass digital filter and a telemetry encoder; the output is transmitted to Earth via the central-station S-band transmitter.

The LSM has two data samplers: the analog-to-digital converter (26.5 samples/second) and the central-station telemetry

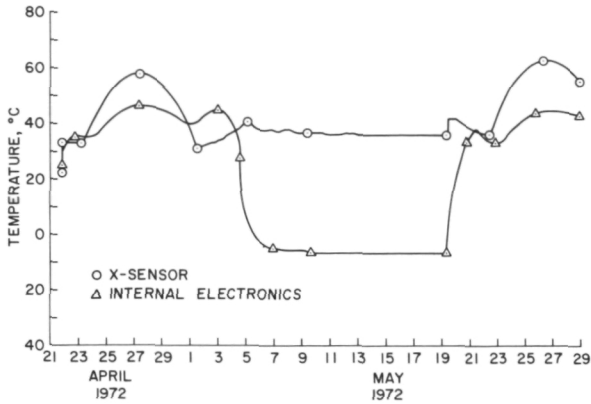


Figure 3.—Temperature inside one of the Apollo 16 LSM flux-gate sensors and inside the electronics box during the first postdeployment lunation of the Apollo 16 instrument.

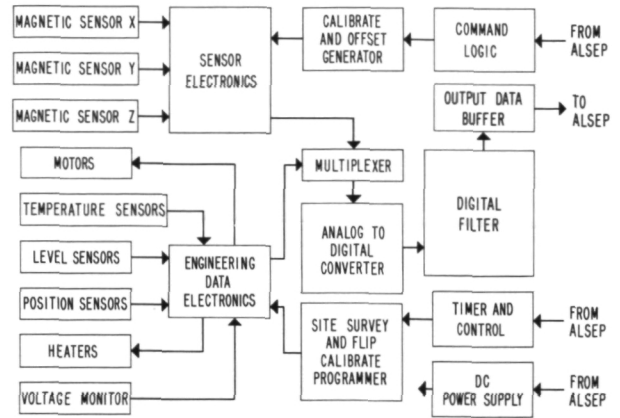


Figure 4.—Functional block diagram for the Apollo LSM electronics.

encoder (3.3 samples/second). The pre-alias filter following the sensor electronics has attenuations of 3 dB at 1.7 Hz, 64 dB at 26.5 Hz, and 58 dB at the Nyquist frequency (13.2 Hz), with an attenuation rate of 22 dB/octave. The four-pole Bessel digital filter limits the alias error to less than 0.5 percent and has less than 1 percent overshoot for a step function response. This filter has an attenuation of 3 dB at 0.3 Hz and 48 dB at the telemetry-sampling Nyquist frequency (1.6 Hz). The phase response is linear with frequency. The response of the entire LSM measurement system to a step function input is shown in figure 5. The digital filter can be bypassed by ground command in order to pass higher frequency information.

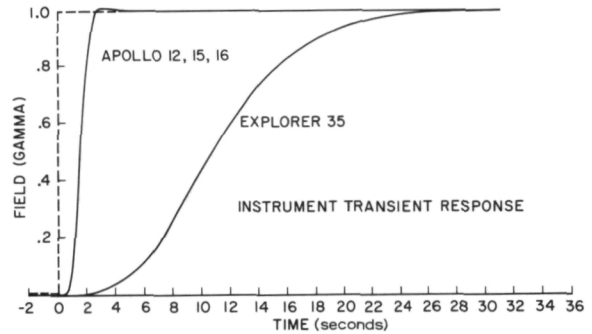


Figure 5.—Laboratory measurements comparing instrument transient responses of the Apollo 12, 15, and 16 lunar surface magnetometers with the Explorer 35 lunar orbiting magnetometer for a 1.0- $\gamma$  step change in the input magnetic field.

### Fluxgate Sensor

Three orthogonal vector components of the magnetic field are measured by three fluxgate sensors designed and fabricated by the U.S. Naval Ordnance Laboratory (ref. 56). The sensor shown schematically in figure 6 consists of a toroidal Permalloy core that is driven to saturation by a sinusoidal current having a frequency of 6000 Hz. The sense winding detects the superposition of the drive-winding magnetic field and the total lunar surface field; as a result, a second har-

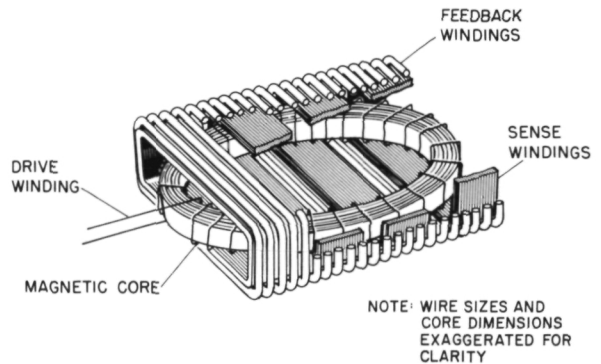


Figure 6.—Simplified view of the ring core magnetometer sensor developed jointly by the U.S. Naval Ordnance Laboratory and NASA/Ames Research Center.

monic of the driving frequency is generated in the sense winding with a magnitude that is proportional to the strength of the surface field. The phase of the second harmonic signal with respect to the drive signal indicates the direction of the surface field with respect to the sensor axis. This output signal is amplified and synchronously demodulated to drive a voltage to the analog-to-digital converter and then through the central-station radio to Earth.

### Data Flow and Mission Operation

The LSM experiment is controlled from the NASA/Johnson Space Center (JSC) by

commands transmitted to the Apollo lunar surface experiments package (ALSEP) from remote tracking stations. The data are recorded on magnetic tape at the remote sites and are also sent directly to JSC for real-time analysis to establish the proper range, offset, frequency response, thermal control, and operating mode.

The Apollo 12 LSM returned useful scientific information from the time of its deployment on day 323 of 1969 to day 256 of 1971. The Apollo 15 LSM operated from its deployment on day 212 of 1971 to day 264 of 1972. The Apollo 16 LSM was deployed on day 112 of 1972 and continues to return useful information at the time of this writing.

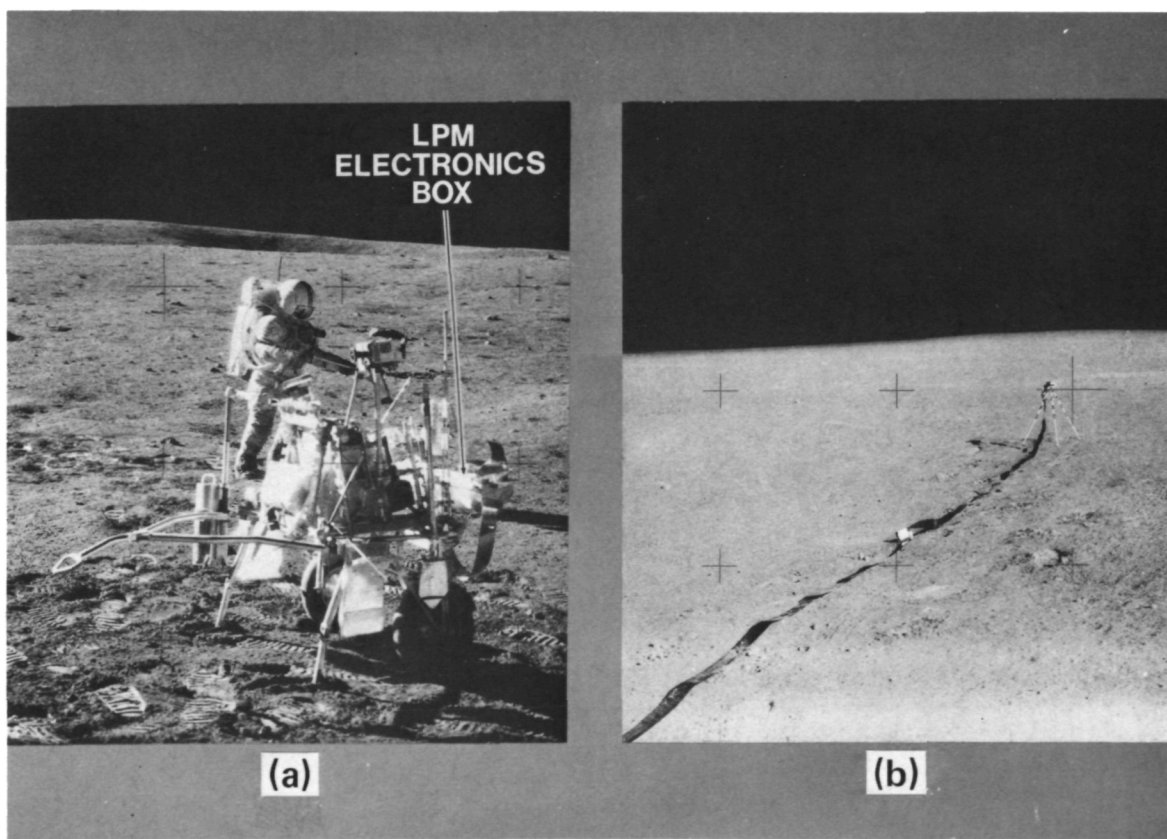


Figure 7.—The Apollo 14 lunar portable magnetometer (LPM), shown (a) stowed aboard the mobile equipment transporter and (b) deployed during a magnetic field measurement. The sensor-tripod assembly is deployed 15 meters from the electronics box, which remains on the mobile equipment transporter so that magnetic fields of the astronaut's suit and other equipment will not be measured by the LPM.

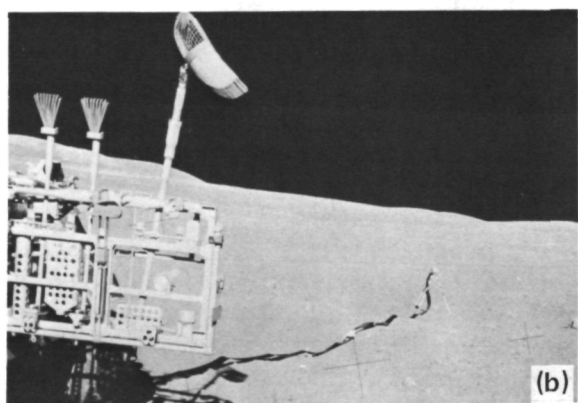
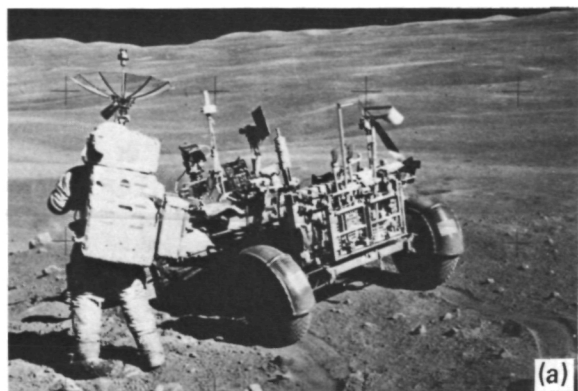


Figure 8.—The Apollo 16 LPM (a) stowed on the lunar roving vehicle and (b) deployed during a magnetic field measurement.

## LUNAR PORTABLE MAGNETOMETER (LPM)

The self-contained LPM is used to measure the steady magnetic field at different points along the lunar traverse of the astronauts. Two portable magnetometers have been deployed on the moon by the Apollo astronauts: one at the Apollo 14 site ( $3.7^\circ$  S,  $17.5^\circ$  W) shown in figure 7, and one at the Apollo 16 landing site ( $9.0^\circ$  S,  $15.5^\circ$  E) shown in figure 8.

The LPM field measurements are a vector sum of the steady remanent field from the lunar crust and of the time-varying ambient fields. The LSM simultaneously measures the time-varying components of the field; these components are later subtracted from the

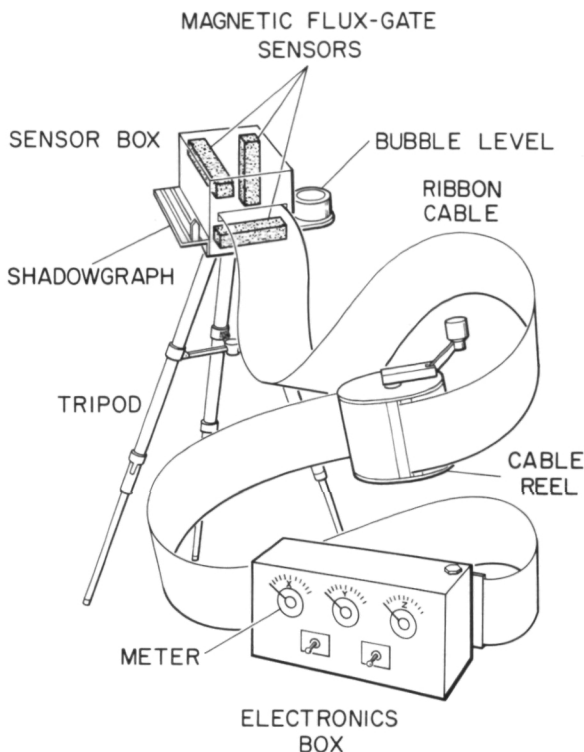


Figure 9.—Schematic diagram of the Apollo 14 LPM. The sensor-tripod assembly is connected by means of a 15-meter ribbon cable to the electronics box, which contains a battery pack, electronics, and visual displays for three magnetic field vector components. Meter displays are used for the Apollo 14 LPM, and digital displays are used for the Apollo 16 LPM.

LPM measurements to give the desired resultant steady field values caused by the magnetized crustal material. The LPM consists of a set of three orthogonal fluxgate sensors mounted on top of a tripod (fig. 9); the sensor-tripod assembly is connected by means of a 15-m ribbon cable to the electronics box, which is mounted on the mobile equipment transporter (Apollo 14) or the lunar roving vehicle (Apollo 16).

The 15-m cable length was determined from magnetic properties tests of the mobile equipment transporter and lunar roving vehicle. The LPM was calibrated by using magnetic reference instruments directly traceable to the U.S. National Bureau of Standards. The pertinent LPM characteristics are listed in table 1.

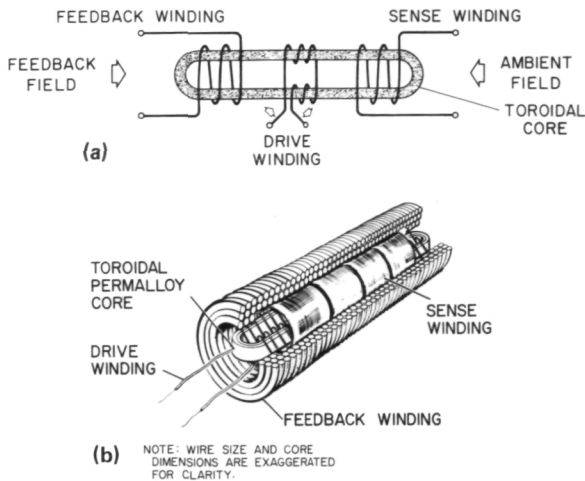


Figure 10.—The fluxgate used in the LPM to measure each of three components of the magnetic field, (a) Functional schematic. (b) Cutaway view of the sensor windings and high-permeability core.

## Fluxgate Sensor

The fluxgate sensor, shown schematically in figure 10 is used to measure the vector components of the magnetic field in the magnetometer experiment. Three fluxgate sensors (refs. 56 and 57) are orthogonally mounted in the sensor block as shown in figure 9. Each sensor (see fig. 10) weighs 18 g and uses 15 mW of power during operation. The sensor consists of a flattened toroidal core of Permalloy that is driven to saturation by a square wave at a frequency  $f_0 = 7250$  Hz. This constant-voltage square wave drives the core to saturation during alternate half cycles and modulates the permeability at twice the drive frequency. The voltage induced in the sense windings is equal to the time rate of change of the net flux contained in the area enclosed by the sense winding. This net flux is the superposition of the flux from the drive winding and the ambient magnetic field. The signal generated in the sense winding at the second harmonic of the drive signal will be amplitude modulated at a magnitude proportional to the ambient magnetic field. The phase of this second harmonic signal with respect to the drive waveform indicates the polarity of the

magnetic field. The sensor electronics amplifies and filters the  $2f_0$  sense-winding signal and synchronously demodulates it to derive a voltage proportional to the ambient magnetic field. After demodulation, the resulting signal is amplified and used to drive the feedback winding to null out the ambient field within the sensor. Operating at null increases thermal stability by making the circuit independent of core permeability variations with temperature.

The sensor block, mounted on the top of a tripod, is positioned 75 cm above the lunar surface. The tripod assembly consists of a latching device to hold the sensor block, a bubble level with  $1^\circ$  annular rings, and a shadowgraph with  $3^\circ$  markings used to align the device along the Moon-to-Sun line.

## Electronics

The magnetometer electronics box is self-contained with a set of mercury cells for power and three digital displays for visual readout of the magnetic field components. A block diagram of the instrument is shown in figure 11. The sensors are driven into saturation by a 7.25-kHz square wave, and a 14.5-kHz pulse is used to demodulate the second harmonic signal from the sense windings. The amplifier output is synchronously demodulated, producing a direct-current output voltage proportional to the amplitude of the ambient magnetic field. This demodulated output is used to drive the feedback wind-

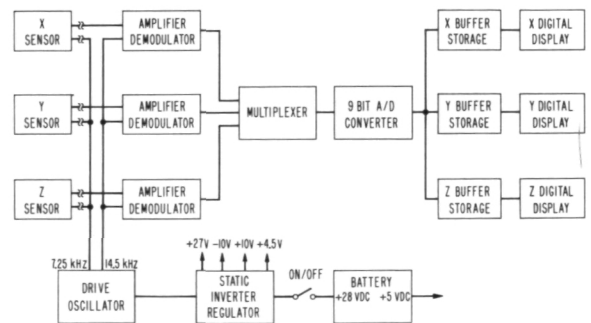


Figure 11.—Functional block diagram of the LPM electronics.

ing of the sensor so that the sensor can be operated at null conditions. The demodulated output from each channel is passed through a low pass filter with a time constant of 20 seconds.

Three meters were used to read the electronics output of the Apollo 14 LPM. The Apollo 16 LPM was actuated by a READ switch which caused the filtered analog signal to be converted to a digital 9-bit binary number. In system operation, the output of the analog-to-digital converter then goes to a storage register for display by the light-emitting diode numeric indicator. Three numeric indicators are used for each axis and read out in octal from 000 to 777 for magnetic field values from  $-256$  to  $+256 \gamma$ .

## Deployment and Operation

The astronaut operation was crucial to the execution of this experiment. The following measurement sequence was conducted: leaving the electronics box on the mobile equipment transporter (Apollo 14) or lunar roving vehicle (Apollo 16), the astronaut deployed the sensor-tripod assembly about 15 meters away, leveling and azimuthally aligning the instrument by bubble level and shadowgraph. The astronaut then returned to the electronics box, turned the power switch on, read the sensor meters (or digital displays) in sequence, and verbally relayed the data back to Earth. At the first deployment site only, two sets of additional readings were taken with the sensor block first rotated  $180^\circ$  about a horizontal axis and then rotated about a vertical axis. These additional readings allowed determination of a zero offset for each axis.

## Explorer 35 Magnetometer

The ambient steady-state and time-dependent magnetic fields in the lunar environment are measured by the Explorer 35 satellite magnetometer. The satellite has an orbital period of 11.5 hrs., an aposelene of 9390 km, and a periselene of 2570 km (fig.

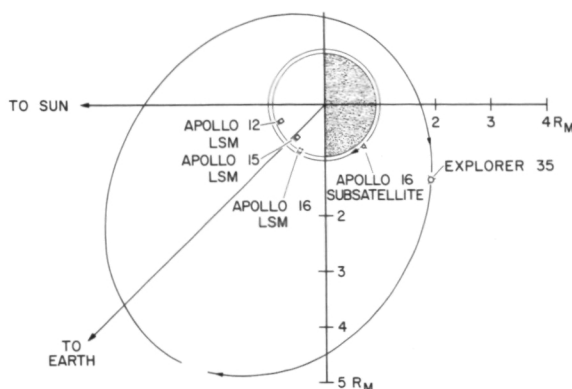


Figure 12.—The Explorer 35 orbit around the Moon, projected onto the solar ecliptic plane. The period of revolution is 11.5 hrs. The Apollo 12, 15, and 16 surface instrument positions and Apollo 16 subsatellite trajectory are shown.

12). Two magnetometers are carried aboard Explorer 35, one provided by NASA/Ames Research Center and the other provided by NASA/Goddard Space Flight Center. Since most of the analysis of lunar internal properties has been carried out with the Ames magnetometer, its characteristics will be considered here. The Explorer 35 Ames magnetometer measures three magnetic field vector components very 6.14 seconds and has an alias filter with 18-dB attenuation at the Nyquist frequency (0.08 Hz) of the spacecraft data-sampling system. This instrument has a phase shift linear with frequency, and its step-function response is slower than that of the Apollo LSM instrument (fig. 5). Further information about the Explorer 35 magnetometer is given by Sonett et al. (ref. 58). Figure 12 also shows the orbit of the Apollo 16 particles and fields subsatellite which carried a magnetometer, and the three lunar surface magnetometers. Additional information on the subsatellite magnetometer is reported by Coleman et al. (refs. 59 and 60).

## The Lunar Magnetic Environment

In different regions of a lunar orbit, the magnetic environment of the Moon can have

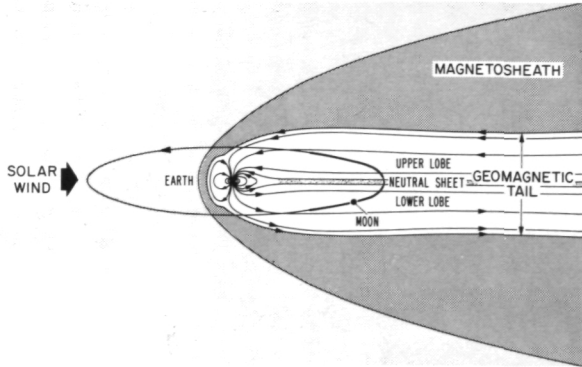


Figure 13.—Magnetic environment of the Moon during a complete lunar orbit, with emphasis on the geomagnetic tail region. The plane of the lunar orbit very nearly coincides with the ecliptic plane of the Earth's orbit. The Earth's permanent dipole field is swept back into a cylindrical region known as the geomagnetic tail; at the lunar distance the field magnitude is  $\sim 10$  gammas or  $10^{-4}$  oersteds. Substructure of the tail consists of two "lobes"; the upper or northward lobe has its magnetic field pointing roughly toward the Earth, whereas the lower lobe field points away from the Earth. The Moon is immersed about four days of each orbit in the tail; the Moon can pass through either or both lobes (accented portion of orbit), depending upon the characteristics of the particular orbit.

distinctly different characteristics (see figure 13). Average magnetic field conditions vary from relatively steady fields of magnitude  $\sim 10 \gamma$  in the geomagnetic tail to mildly turbulent fields averaging  $\sim 5 \gamma$  in the free-streaming solar plasma region, to turbulent fields averaging  $\sim 8 \gamma$  in the magnetosheath. Average solar wind velocity is  $\sim 400$  km/s in a direction approximately along the Sun-Earth line.

Various induced lunar and plasma-interaction fields are assumed to exist at the lunar surface; for reference, we write the sum of these fields as

$$\underline{B}_A = \underline{B}_E + \underline{B}_R + \underline{B}_\mu + \underline{B}_P + \underline{B}_T + \underline{B}_D + \underline{B}_F \quad (1)$$

Here  $\underline{B}_A$  is the total magnetic field measured on the surface by an Apollo lunar surface magnetometer;  $\underline{B}_E$  is the total external (solar or terrestrial) driving magnetic field measured by the Explorer 35 and Apollo 15 subsatellite lunar orbiting magnetometers while

outside the antisolar lunar cavity;  $\underline{B}_R$  is the steady remanent field at the surface site;  $\underline{B}_\mu$  is the magnetization field induced in permeable lunar material;  $\underline{B}_P$  is the poloidal field caused by eddy currents induced in the lunar interior by changing external fields;  $\underline{B}_T$  is the toroidal field corresponding to unipolar electrical currents driven through the Moon by the  $V \times \underline{B}_E$  electric fields;  $\underline{B}_D$  is the field associated with the diamagnetic lunar cavity; and  $\underline{B}_F$  is the field associated with the hydromagnetic solar wind flow past the Moon.

The interaction of the solar wind with the Earth's permanent dipole field results in formation of the characteristic shape of the Earth's magnetosphere; the solar wind in effect sweeps the Earth's field back into a cylindrical region (the geomagnetic tail) on the Earth's antisolar side. The Earth's field magnitude is about  $30\,000 \gamma$  at the equator; in the geomagnetic tail the field decreases with distance from the earth with a radial dependence expressible as  $R^{-0.736}$  (ref. 61). At the distance where the Moon's orbit intersects the tail, the field magnitude is  $\sim 10 \gamma$ . The Moon is in the geomagnetic tail for about four days of each 29.5-day lunation (period between successive full Moons). Substructure of the tail consists of two "lobes": the upper or northward lobe has its magnetic field pointing roughly toward the Earth, whereas the lower lobe field points away from the Earth. The Moon can pass through either or both lobes, depending upon the characteristics of the particular orbit, the geomagnetic dipole axis orientation, and perturbations of the geomagnetic field by solar wind pressures. When the Moon is passing through a quiet region of the geomagnetic tail, solar wind interaction fields ( $\underline{B}_T$ ,  $\underline{B}_D$ , and  $\underline{B}_F$ ) and the induced poloidal lunar field  $\underline{B}_P$  are negligible, and the total field at the lunar surface is

$$\underline{B}_A = \underline{B}_E + \underline{B}_\mu + \underline{B}_R \quad (2)$$

The induced magnetic field  $\underline{B}_\mu$  is dependent on the relative magnetic permeability distribution of the lunar sphere and is proportional to the external magnetic field  $\underline{B}_E$ .

Therefore, when  $B_E = 0$ ,  $B_A = B_R$  and the Apollo magnetometer measures the steady remanent field alone. Once  $B_R$  is known, the relative magnetic permeability of the Moon  $\mu/\mu_0$  can be calculated.

A different set of field terms in equation (1) is dominant when the Moon is immersed in free-streaming solar wind and the magnetometer is on the lunar sunlit side.  $B_D \rightarrow 0$  outside the cavity, and the global fields  $B_\mu$  and  $B_T$  can be neglected in comparison to  $B_P$  (ref. 38). The interaction field  $B_F$  has been found to be important during times of high solar wind particle density (ref. 29); therefore the interaction term  $B_F$  is not to

be assumed negligible in general, and equation (1) becomes

$$B_A = B_P + B_E + B_R + B_F \quad (3)$$

At low frequencies ( $\leq 3 \times 10^{-4}$  Hz),  $B_P \rightarrow 0$  and the interaction field  $B_F$  can be investigated.

When the magnetometer is located on the dark (antisolar) side of the Moon, it is generally isolated from solar plasma flow and  $B_P \rightarrow 0$ . Then for dark side data, equation (3) reduces to

$$B_A = B_P + B_E + B_R \quad (4)$$

where cavity effects ( $B_D$ ) are neglected to a

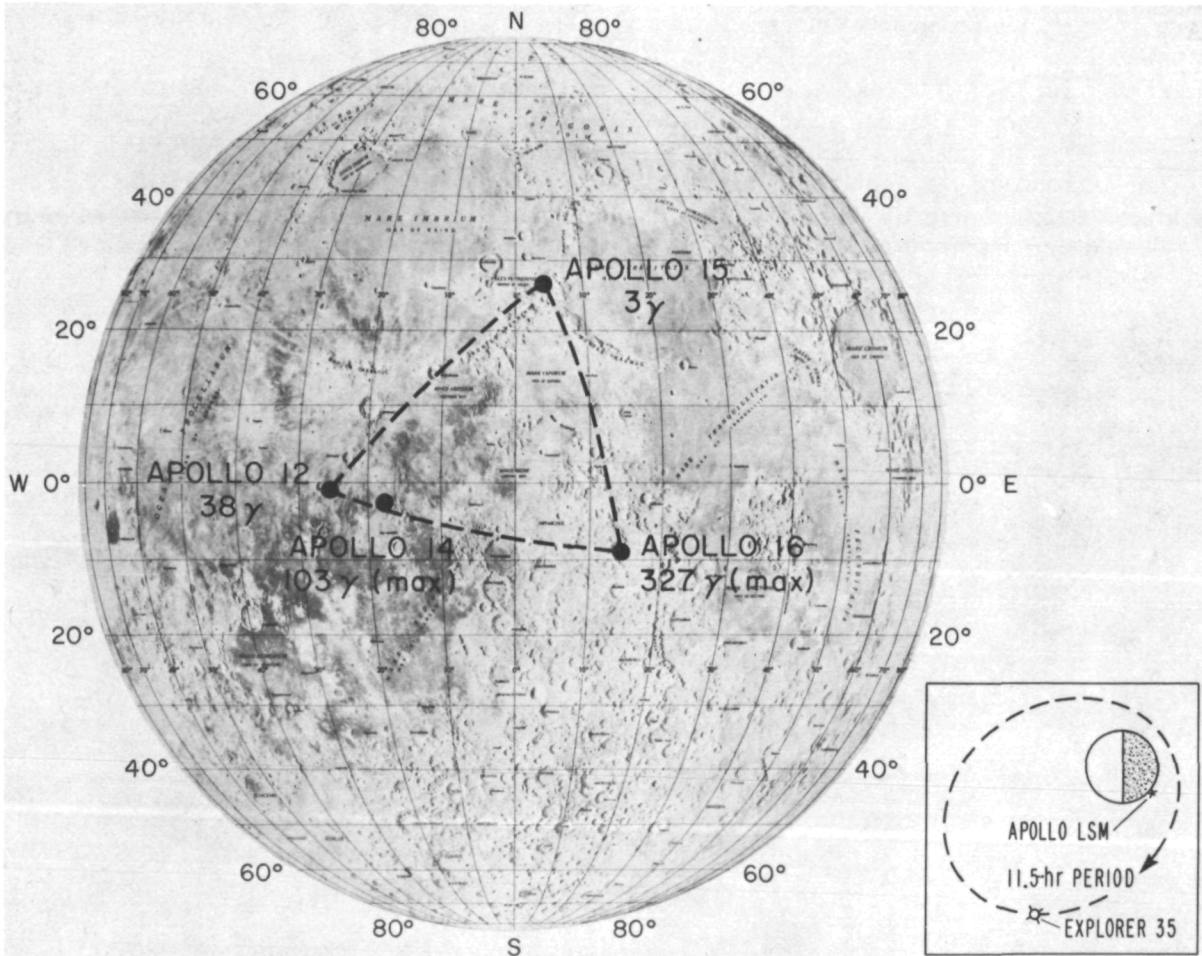


Figure 14.—Apollo magnetometer network on the lunar surface. Maximum remanent magnetic fields measured at each landing site are shown.

first approximation for measurements made near lunar midnight (ref. 38). After  $\underline{B}_R$  has been calculated from geomagnetic tail data, only the poloidal field  $\underline{B}_P$  is unknown. Equation (4) can then be solved for certain assumed lunar models, and curve fits of data to the solution determine the model-dependent conductivity profile  $\sigma(R)$ . Furthermore, electrical conductivity is related to temperature, and the lunar interior temperature can be calculated for assumed lunar material compositions.

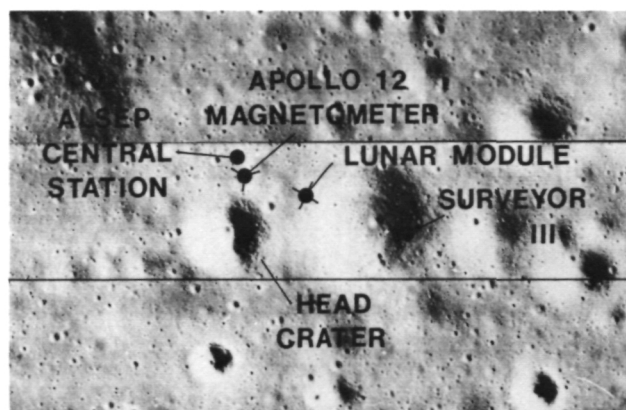
## Lunar Remanent Magnetic Fields

The permanent magnetic fields of the Moon have been investigated by use of surface magnetometer measurements at four Apollo sites (see fig. 14) and the U.S.S.R. Lunokhod II site; orbital measurements from Explorer 35 and two Apollo subsatellite magnetometers; and natural remanent magnetization measurements of returned lunar samples. Lunar remanent field measurements by Apollo surface magnetometers will be em-

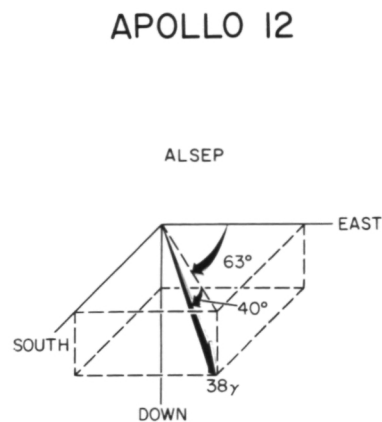
phasized in this paper. Sample magnetization measurements have been reviewed elsewhere (refs. 62-65); orbital results have been reported by Mihalov et al. (ref. 25), Sonett and Mihalov (ref. 66), Coleman et al. (refs. 26, 59, and 60), Sharp et al. (ref. 27), and Russell et al. (refs. 28 and 34).

## SURFACE SITE FIELD MEASUREMENTS

Analyses of Apollo 11 lunar samples first demonstrated the presence of a natural remanent magnetization (NRM) in the lunar surface material. This magnetization ranges from  $10^{-3}$  to  $10^{-7}$  gauss  $\text{cm}^3 \text{g}^{-1}$  and most likely arises from the thermoremanent magnetization of metallic iron grains (ref. 65). The discovery of NRM in the lunar samples, which was a surprise to most scientists, did not lead to the expectation that the magnetization would be ordered on sufficiently large scale to produce localized magnetic fields. Also, measurements from orbiting magnetometers had not been interpreted as indicating the presence of permanent lunar fields



(a)



(b)

Figure 15.—Lunar remanent magnetic field measured at the Apollo 12 site in Oceanus Procellarum. (a) Lunar Orbiter photograph showing the Apollo 12 landing site and location of the surface magnetometer where the remanent field measurements were made. (b) Magnitude and orientation of the measured vector magnetic field.

prior to the Apollo 12 landing in November 1969.

However, a local remanent magnetic field was measured by the first (Apollo 12) lunar surface magnetometer, which was deployed on the eastern edge of Oceanus Procellarum. The permanent field magnitude was measured to be  $38 \pm 3$  gammas and was attributed to local sources composed of magnetized sub-surface material (refs. 23 and 24; see fig. 15). A remanent field this large was generally unexpected, and the origin of magnetized regions on the Moon yet remains a central problem in lunar magnetism. Subsequent to this measurement of an intrinsic lunar magnetic field, surface magnetometers have measured fields at the Apollo 14, 15, and 16 sites. Fields of  $103 \pm 5$  and  $43 \pm 6$  gammas, at two sites located about a kilometer apart, were measured by the Apollo 14 Lunar Portable Magnetometer (LPM) at Fra Mauro (see fig. 16). A steady field of  $3.4 \pm 2.9$  gammas was measured near Hadley Rille by the Apollo 15 LSM (see fig. 17). At the Apollo 16 landing site both a portable and stationary magnetometer were deployed; magnetic fields ranging between 112 and 327 gammas were measured at five different lo-

cations over a total distance of 7.1 kilometers at the Descartes landing site. These are the largest lunar fields yet measured. A schematic representation of the measured field vectors is shown in figure 18. All the vectors have components pointing downward except the one at Site 5 near Stone Mountain, which points upward. This suggests, among other possibilities, that the material underlying Stone Mountain has undergone different geological processes than that underlying the Cayley Plains and North Ray Crater. In fact, Strangway et al. (ref. 67) proposed the possibility that the light-colored, relatively smooth Cayley formation is magnetized roughly vertically; the difference in the vertical component at site 5 was explained as an edge effect at the Cayley Plains-Stone Mountain boundary.

The similarities between the Apollo 12 and 14 field measurements (viz, all vectors are pointed down and toward the south, and have magnitudes that correspond to within a factor of 3) and the proximity of the two landing sites (see fig. 14) suggest that the two Apollo 14 sites and possibly the Apollo 12 site are located above a near-surface slab of material that was uniformly magnetized

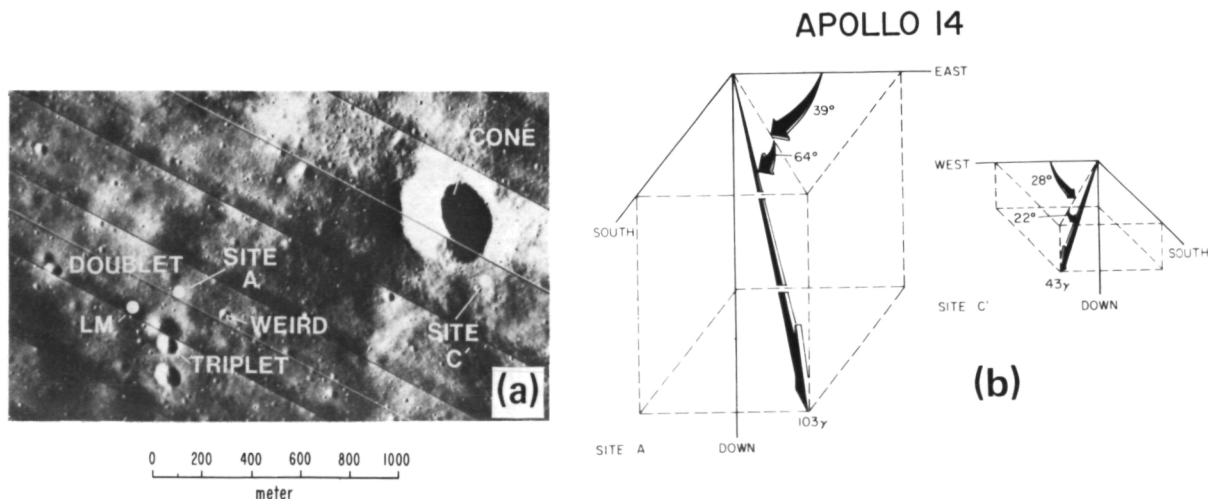


Figure 16.—Lunar remanent magnetic fields measured at the Apollo 14 site at Fra Mauro. (a) Lunar Orbiter photograph showing the Apollo 14 landing site and the locations of sites A and C where the lunar portable magnetometer measurements were made. (b) Magnitude and orientation of the measured remanent magnetic fields.

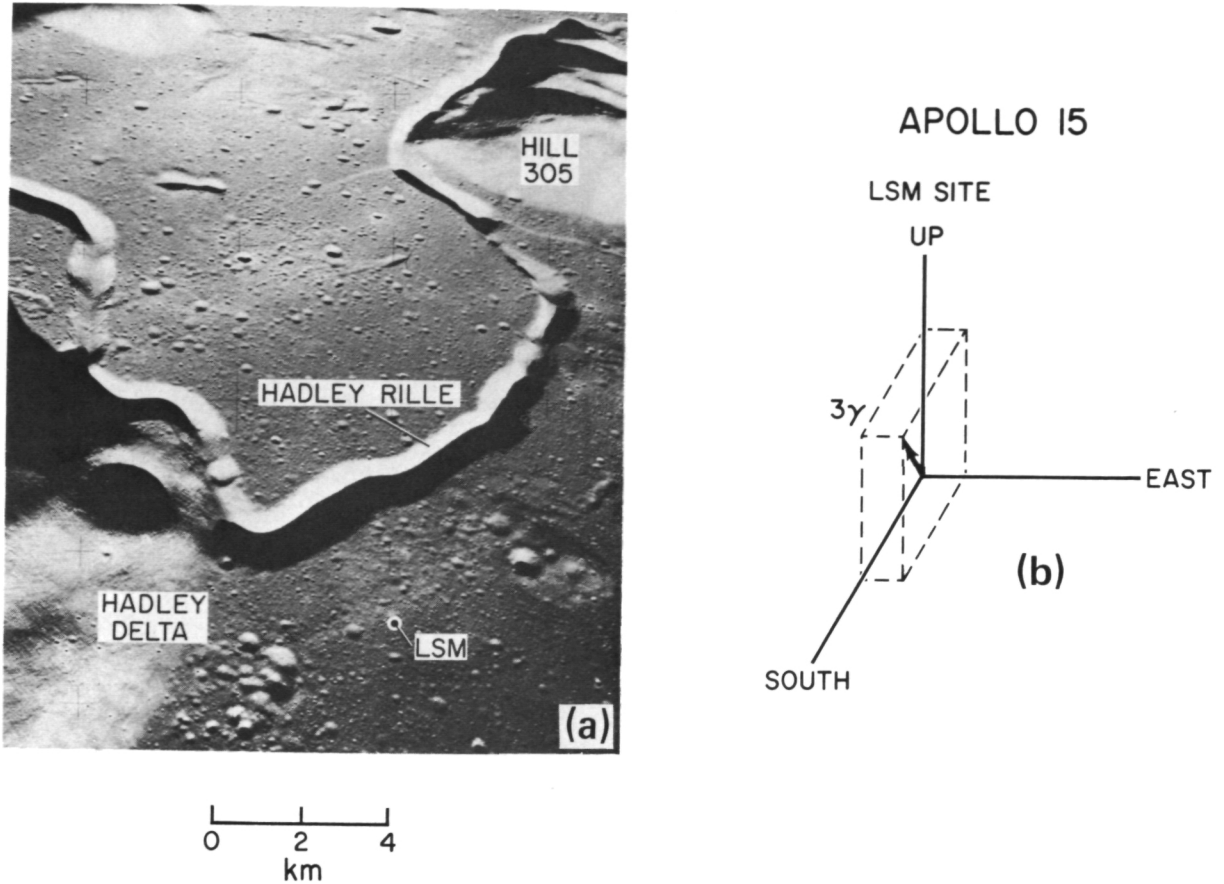
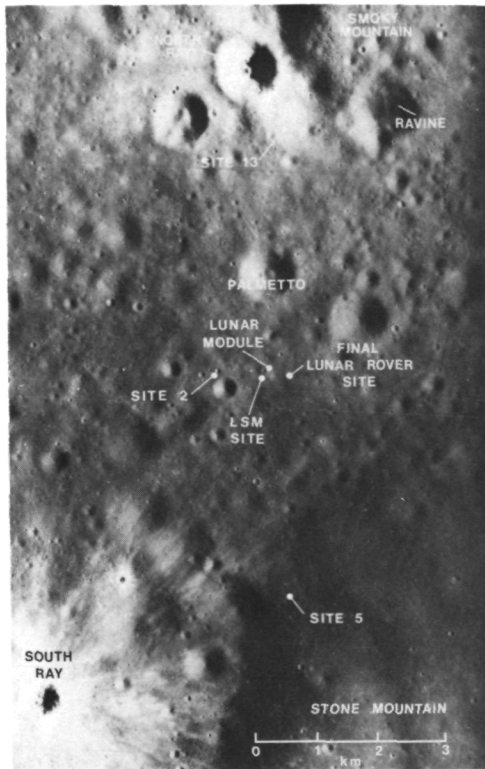


Figure 17.—Lunar remanent magnetic field measured at the Apollo 15 site near Hadley Rille. (a) Photograph showing the Apollo 15 landing site and location of the surface magnetometer where the remanent field measurement was made. (b) Magnitude and orientation of the measured remanent magnetic field.

at one time. Subsequently the magnetization in the slab was perhaps altered by local processes, such as tectonic activity or fracturing and shock demagnetization from meteorite impacts. This latter process is graphically illustrated in figure 19. The Apollo 12 and 14 steady magnetic fields could also originate in surface or subsurface dipolar sources, such as meteoroid fragments or ore bodies. Another possibility is that the region was subjected to a uniform magnetic field but that various materials with differing coercivities were magnetized to different strengths. Another model might involve a slow variation in the direction of the ambient field, causing regions that passed through the Curie temperature at different times to

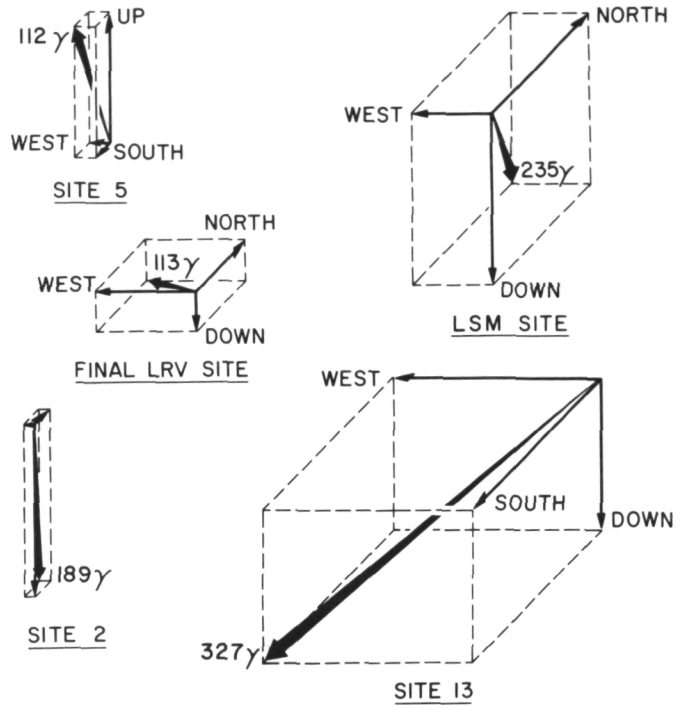
be magnetized in different directions. A summary of all remanent lunar fields measured by the magnetometers deployed on the surface is given in table 2, and the network of surface sites at which remanent fields have been measured is shown in figure 14.

Information on the scale sizes of the permanently magnetized regions near Apollo landing sites is given by gradient measurements of the lunar surface magnetometers, the spacing of vector measurements over the lunar surface, the known interaction properties of these remanent fields with the solar wind plasma, and limits imposed by satellite measurements. The field gradient in a plane parallel to the lunar surface is less than the instrument resolution of 0.13 gamma/meter



(a)

APOLLO 16



(b)

Figure 18.—Lunar remanent magnetic fields measured at the surface Apollo 16 Descartes site. (a) Photograph showing the Apollo 16 landing site, the location of the surface magnetometer, and the traverse positions where the portable magnetometer was deployed. (b) Magnitude and orientation of the measured vector remanent magnetic fields.

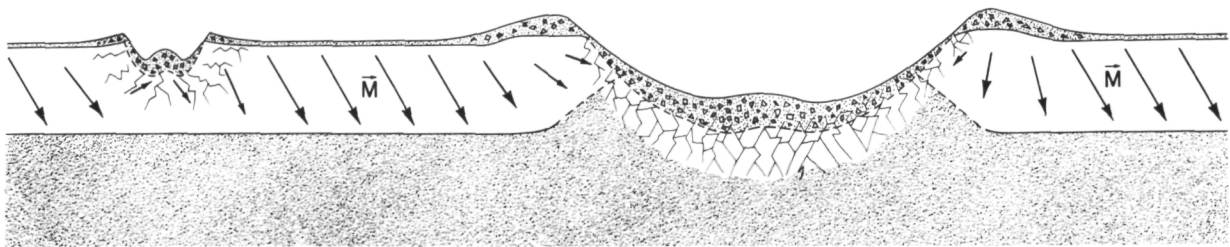


Figure 19.—Conceptual diagram showing disruption of a previously uniformly magnetized subsurface layer by meteorite impact. The vectors ( $\vec{M}$ ) represent the direction and magnitude of remanent magnetization in the layer.

Table 2.—*Summary of Lunar Surface Remanent Magnetic Field Measurements*

Site	Coordinates, Degrees	Field Magnitude, Gammas	Magnetic-Field Components, Gammas		
			Up	East	North
<b>Apollo 16:</b>					
ALSEP Site	8.9°S, 15.5°E	235 ± 4	-186 ± 4	-48 ± 3	+135 ± 3
Site 2		189 ± 5	-189 ± 5	+3 ± 6	+10 ± 3
Site 5		113 ± 4	+104 ± 5	-5 ± 4	-40 ± 3
Site 13		327 ± 7	-159 ± 6	-190 ± 8	-214 ± 6
LRV Final Site		112 ± 5	-66 ± 4	-76 ± 4	+52 ± 2
<b>Apollo 15:</b>					
ALSEP Site	26.1°N, 3.7°E	3.4 ± 2.9	+3.3 ± 1.5	+0.9 ± 2.0	-0.2 ± 1.5
<b>Apollo 14:</b>					
Site A	3.7°S, 17.5°W	103 ± 5	-93 ± 4	+38 ± 5	-24 ± 5
Site C'		43 ± 6	-15 ± 4	-36 ± 5	-19 ± 8
<b>Apollo 12:</b>					
ALSEP Site	3.2°S, 23.4°W	38 ± 2	-25.8 ± 1.0	+11.9 ± 0.9	-25.8 ± 0.4

at the Apollo 12 and 15 sites. At Apollo 14 a field difference of 60  $\gamma$  was measured at two sites located 1.1 km apart. Gradient measurements and the absence of changes in the permanent field at the sites after lunar module ascent demonstrated that the field sources are not magnetized artifacts.

The scale size of the Apollo 12 remanent field has been calculated from local gradient and Explorer 35 measurements to be from 2 km to 200 km (ref. 29). For the Apollo 16 field, portable magnetometer measurements over the lunar roving vehicle traverse showed that the scale size for the field was greater than 5 km; the Apollo 16 subsatellite magnetometer showed no anomalous field attributable to the Descartes area at orbital altitude, implying a surface field scale size upper limit of 100 km. Therefore, the Apollo 16 remanent field scale size is between 5 and 100 km.

## ORIGIN OF THE LUNAR REMANENT MAGNETIZATION

From the beginning of the Apollo missions the origin of the lunar remanent fields has

been of great interest and there has been no shortage of mechanisms proposed to explain the origin of the lunar fields and remanence. Many authors have discussed various aspects of natural remanent magnetization (NRM) in the lunar surface material (e.g., refs. 22, 68, and 69). Possible source mechanisms for the remanent fields have been reviewed by Dyal et al. (refs. 70 and 72), Strangway et al. (ref. 71), and in detail by Fuller (ref. 65). Some of these possible mechanisms are discussed briefly here and displayed schematically in figures 20 and 21.

## Large Solar or Terrestrial Field

The thermoremanent magnetization of the near-surface lunar material (such as might be responsible for the remanent fields measured by the surface and subsatellite magnetometers) was probably accomplished by the cooling of crustal material on a scale of tens of kilometers in a relatively steady external magnetic field of a few thousand gammas. It is possible that the Sun was the source of the external magnetic field (ref. 19). The early solar field may have been greatly en-

hanced during an early T-Tauri solar phase, as suggested by Sonett et al. (ref. 73), although at the lunar orbit such a field was probably even more variable than it is at the present time. A terrestrial field increase greater than 100 times its present value would probably be necessary to magnetize lunar material at the present-day lunar orbit. Such a large terrestrial field is not indicated by paleomagnetic studies. For an ancient terrestrial field of present-day magnitude, the Moon would have to have approached to within 2 to 3 Earth radii, close to the Roche limit (refs. 16 and 74) to be subjected to the necessary field strength. All of the alternatives for these hypotheses seem to have shortcomings.

### Iron Core Dynamo

For this mechanism a whole-Moon field results from the self-generating dynamo action

of a small iron core (refs. 75 and 76). The dynamo is assumed to have been active 3 to 4 billion years ago when surface rocks and breccias were formed. After the thermoremanent magnetization was established in the upper crust material, as it cooled through the Curie temperature, the dynamo turned off. Subsequently, meteorite impacts on the magnetized surface randomized the field's sources by a gardening process (see fig. 19) and destroyed the whole-body magnetization in the crust. The core dynamo hypothesis also has its shortcomings. In the first place it is not clear that even the most efficient dynamo mechanism in a lunar core of limited size would be self-sustaining at rotational speeds for which the Moon could hold together (ref. 77). In addition, it is doubtful that a dynamo, if ever operating, could produce the surface fields to explain the thermoremanent magnetization of some lunar samples (refs. 20 and 77).

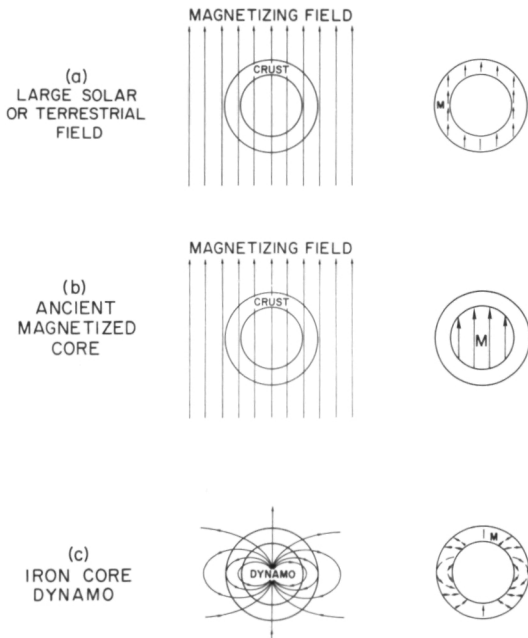


Figure 20.—Schematic representation of some global mechanisms proposed to explain the origin of lunar remanent magnetic fields. (a) Large solar or terrestrial field. (b) Ancient magnetized core. (c) Iron core dynamo. Descriptions of the mechanisms are given in the text.

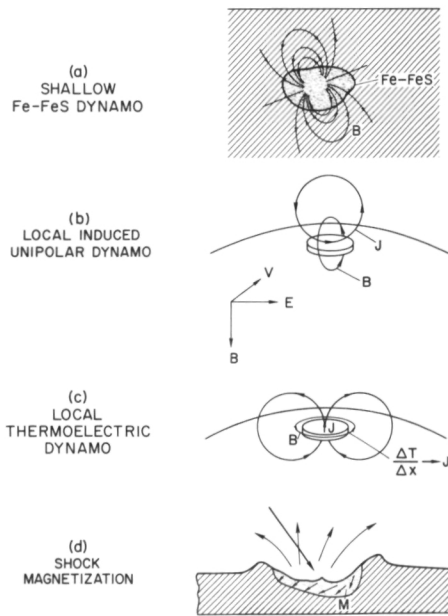


Figure 21.—Schematic representation of some local mechanisms proposed to explain the origin of lunar remanent magnetic fields. (a) Shallow Fe-FeS dynamo. (b) Local induced unipolar dynamo. (c) Local thermoelectric dynamo. (d) Shock magnetization. Descriptions of the mechanisms are given in the text.

## Ancient Magnetized Core

Urey and Runcorn (ref. 78) and Strangway et al. (refs. 64 and 71) have suggested that near-surface material may have been magnetized by the field of a lunar core which had been previously magnetized by one of several possible means: (1) magnetization achieved isothermally by a strong transient field, (2) viscous remanent magnetization by a weak field applied over a long period, (3) depositional remanent magnetization during early lunar formation in a weak field, or (4) thermoremanent magnetization of the core by cooling through the Curie point in a weak field. If the Moon formed in a cold state, neither accretion nor radioactivity would necessarily have raised the temperature of the deep interior above the Curie point of iron, with accompanying loss of magnetization, until 4.1 to 3.2 billion years ago. In the outer shell, perhaps 200 to 400 km thick, partial melting could easily have been realized during later stages of accretion. During the crystallization of the crustal rocks in the magnetic field of the core, they obtained a thermoremanence. Subsequently, radioactive heating in the interior raised the core temperature above the Curie point, resulting in loss of the magnetization in the core.

## Shallow Fe-FeS Dynamo

A model related to the lunar core dynamo is one hypothesizing small pockets of iron and iron sulfide (Fe-FeS) melt a few hundred kilometers below the surface (ref. 79) which act as small localized dynamos. The proponents of this mechanism suggest that these "fescons" are about 100 km in diameter. A variation of this local dynamo idea is suggested by Smolychowski (ref. 80) wherein a thin layer of molten basalt generates the field. The existence of such local source regions for magnetic field should be evident once the surface fields have been mapped over more of the lunar surface. However, the recently discovered asymmetry in the electromagnetic field fluctuations at the

Apollo 15 landing site (ref. 81) could be due to such a highly conducting subsurface body.

## Local Induced Unipolar Dynamo

The solar wind transports magnetic fields past the Moon at velocities  $V$  of approximately 400 km/s; the corresponding  $V \times B$  electric field causes currents to flow along paths of high electrical conductivity (refs. 19 and 35) such as molten mare regions, with the highly conducting solar wind plasma completing the circuit back to the lunar interior. The fields associated with these currents magnetize the materials as they cool below the Curie temperature. Because this induction mechanism has the strongest influence while the hot region is sunlit, an average preferred direction is associated with  $V$ . However, the  $V \times B$  induction model requires solar wind magnetic fields or velocities much higher than the present-day Sun provides.

## Local Thermoelectrically Driven Dynamo

Dyal et al. (ref. 45) have proposed a mechanism of thermoelectrically driven currents to account for remanent fields. Thermoelectric potential is a function of the thermal gradient and electrical properties of the geological material. For the mechanism, a mare basin is modeled by a disk which has an axial temperature gradient. Thermal gradients in the cooling mare lava could produce a Thomson thermoelectromotive force which would drive currents axially through the mare disk. The solar wind plasma, highly conducting along magnetic field lines, could provide a return path to complete the electrical circuit from the top surface of the lava to the lunar surface outside the mare and back into the mare through the lunar interior. The upper limit of the fields generated in terrestrial materials by this process is a few thousand gammas. Such fields near a mare disk would produce thermoremanent magnetization in the Moon of magnitudes measured in lunar samples. This mechanism

awaits experimental verification using materials characteristic of lunar mare composition.

### Shock Magnetization

Anisotropic compression of rocks by meteorite impacts is suggested by Nagata et al. (ref. 82) as a means of inducing a remanence in certain samples which they studied magnetically. This piezo-remanent magnetization can be significantly large even when the external field is very weak (e.g., the solar wind field) if the uniaxial compression is very large. This mechanism is appealing since it relies on a well-established lunar process and may explain some correlation between craters and magnetic anomalies (ref. 27), but the details remain undeveloped.

### Local Currents from Charged Particle Transport

Any process which results in plasma flow near the lunar surface may generate strong local currents and magnetic fields. Cap (ref. 83), for example, has shown that ionized volcanic ash flows may produce fields up to  $10^3$  gammas. As another example, Nagata et al. (ref. 82) proposed the idea that lightning may be generated as a result of exploding dust clouds from meteorite impacts. The large currents associated with an electrical discharge could produce transient magnetic fields up to 10 or 20 gauss, resulting in isothermal remanent magnetization of local material.

At this time it is difficult to determine which of the above mechanisms is responsible for the lunar sample NRM. Of course, several (or none) of these hypotheses may explain the phenomenon. It seems to the authors that the locally active mechanisms are preferable over the global mechanisms because of the very low upper limit on the permanent global magnetic dipole moment and the apparently random nature of the local fields on the scale of tens of kilometers. Certainly a large amount of work remains

to be carried out using the available lunar data, simulations in the laboratory, and future orbital measurements before preferred hypotheses can be identified with any degree of certainty.

### REMANENT FIELD INTERACTION WITH THE SOLAR WIND

Compression of the remanent lunar magnetic field by the solar wind has been measured at the Apollo 12 and 16 sites. Simultaneous surface magnetic field and plasma data show, to first order, a compression of the remanent field in direct proportion to the solar wind pressure as schematically illustrated in Figure 22.

In order to study the compression of the remanent field, it is advantageous to define a field  $\Delta B$  as

$$\Delta B = B_A - (B_E + B_R), \quad (5)$$

where  $B_A$  is the total surface magnetic field, measured by an Apollo lunar surface magnetometer;  $B_E$  is the extralunar (solar) driving magnetic field, measured by the lunar orbiting Explorer 35 magnetometer; and  $B_R$  is the steady remanent field at the site due to magnetized material. For low frequencies, i.e., 1-hour averages of magnetic

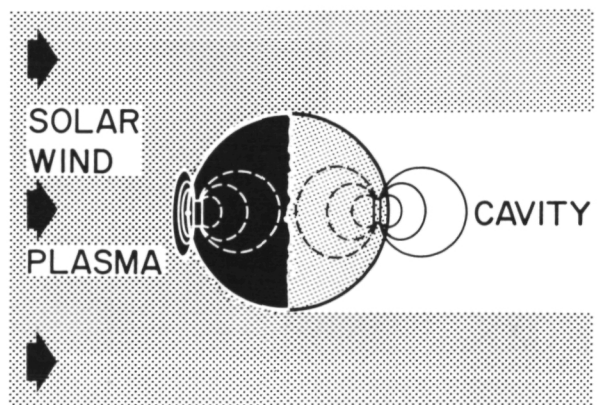


Figure 22.—Schematic representation of remanent field compression by a high-density solar wind plasma. The remanent field is unperturbed during nighttime (antisolar side), while on the sunlit side it is compressed.

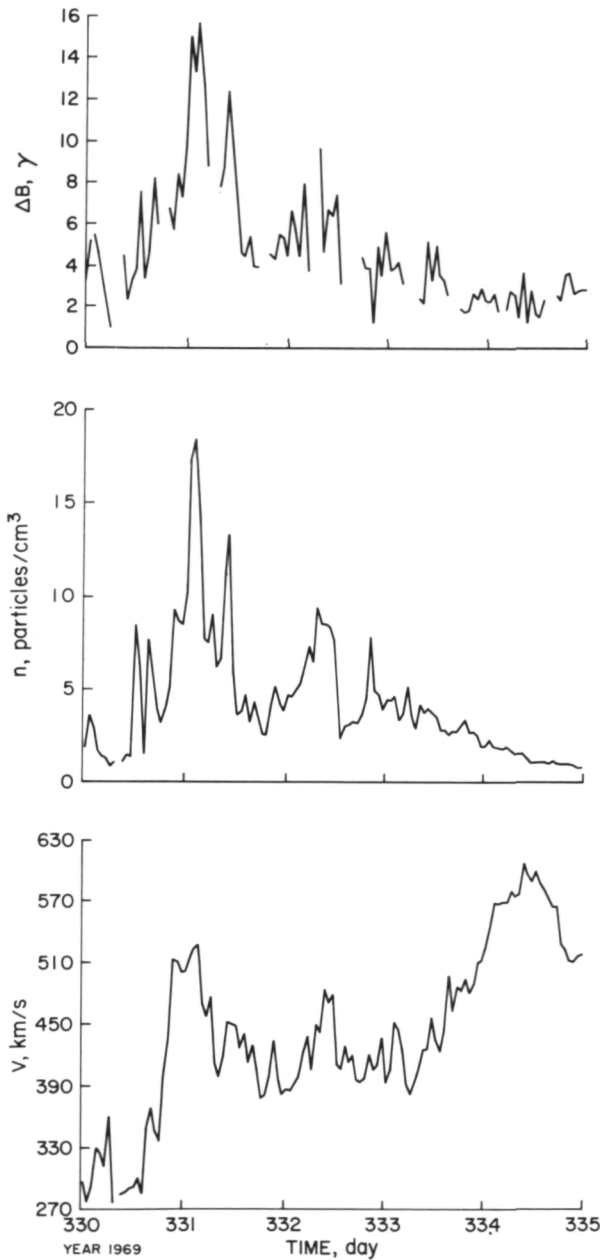


Figure 23.—Simultaneous graphs of magnitude of the vector  $\Delta B = B_A - (B_E + B_R)$ , plasma density, and plasma velocity.  $B_A$  is the total surface field measured by the Apollo 12 lunar surface magnetometer,  $B_E$  is the extralunar field measured by lunar orbiting Explorer 35, and  $B_R$  is the remanent field at the Apollo 12 site.

and solar wind data, the eddy-current poloidal field can be neglected and equation (5) contains all the vector fields, which are dominant at the lunar surface.

We shall show that to first order  $\Delta B$  is the vector change in the steady remanent field due to the solar wind pressure. Figure 23 shows simultaneous 1-hour average plots of the magnitude of the vector field difference  $\Delta B$ , solar wind proton density  $n$ , and solar wind velocity magnitude  $V$  measured at the Apollo 12 site. All data are expressed in the surface coordinate system ( $\hat{x}$ ,  $\hat{y}$ ,  $\hat{z}$ ) which has its origin at the Apollo 12 magnetometer site;  $\hat{x}$  is directed radially outward from the surface while  $\hat{y}$  and  $\hat{z}$  are tangent to the surface, directed eastward and northward,

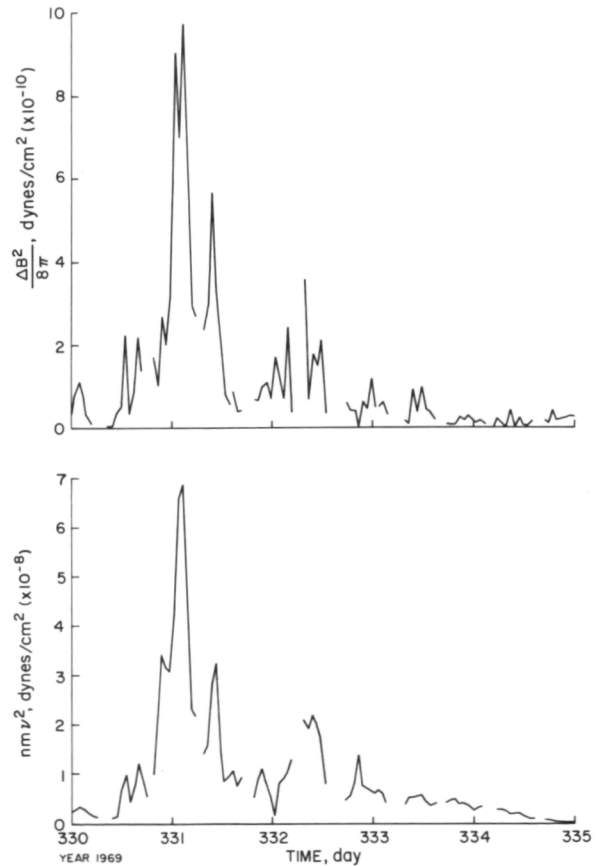


Figure 24.—Simultaneous plots of the magnetic field pressure difference  $\Delta B^2/8\pi$  and solar wind bulk pressure  $nmv^2$  at the Apollo 12 surface site, showing the correlation between the pressures.

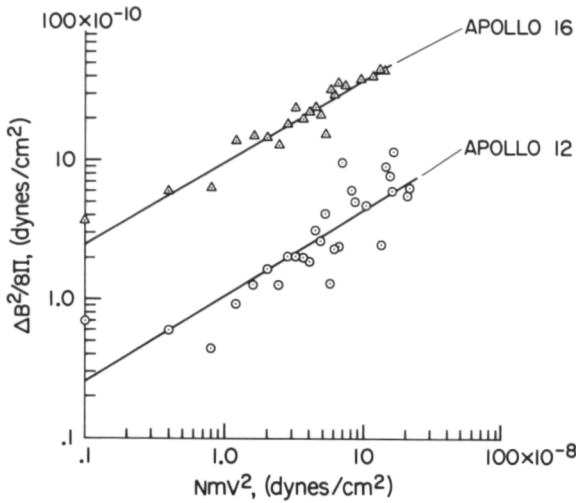


Figure 25.—Magnetic energy density versus plasma energy density at two Apollo sites which have different remanent magnetic fields. Energies are defined in figure 24. Uncompressed remanent field magnitudes are 38  $\gamma$  at Apollo 12 and 234  $\gamma$  at Apollo 16. Apollo 12 magnetometer data are plotted versus Apollo 12 solar wind spectrometer (SWS) data, while Apollo 16 magnetometer data are plotted versus Apollo 15 SWS data. The SWS data are available by courtesy of C. W. Snyder and D. R. Clay of the Jet Propulsion Laboratory.

respectively. Components of the steady remanent field at the Apollo 12 site have been determined (ref. 38) to be  $B_{Rx} = -25.8 \gamma$ ,  $B_{Ry} = +11.9 \gamma$ , and  $B_{Rz} = -25.8 \gamma$ . By inspection we see a strong relationship between the magnitude  $\Delta B$  and plasma proton density ( $n$ ); no such strong correlation, however, is apparent between  $\Delta B$  and velocity  $V$  alone.

The ratio of plasma pressure to total magnetic pressure is expressed

$$\beta = \frac{nmV^2}{B_{ST}^2/8\pi} \quad (6)$$

where  $B_{ST} = B_s + \Delta B$  is the total surface compressed field. During times of maximum plasma pressure shown in figure 24, we calculate  $\beta = 5.9$ ;  $\beta \leq 1$  would imply that the field had been compressed to the stagnation magnitude required to stand off the solar wind and possibly form a local shock. Compression of the remanent field alone therefore does not cause the stagnation condition to be reached during the time period of these data; however, at high frequencies the induced poloidal field  $B_p$  is also compressed ( $\Delta B = B_p + B_r$  in equation (3)), and thus it is possible that the stagnation pressure is reached for short time periods. Total surface fields of over 100 gammas have been observed (ref. 84) when large solar field transients pass the Moon; therefore a shock

could be formed temporarily at the Apollo 12 site (as well as at the Apollo 14 and 16 sites).

The nature of the correlation between magnetic field and plasma pressures is further illustrated in figure 25, which shows data from several lunations at the Apollo 12 and 16 LSM sites. The pressures are related throughout the measurement range. The magnitudes of magnetic pressure changes at the Apollo 12 and Apollo 16 LSM sites are in proportion to their unperturbed steady field magnitudes of 38  $\gamma$  and 234  $\gamma$ , respectively.

### Global Magnetization Induction: Magnetic Permeability and Iron Abundance

Magnetic permeability and iron abundance of the Moon are calculated by analysis of magnetization fields induced in the permeable material of the Moon. When the Moon is immersed in an external field it is magnetized; the induced magnetization is a function of the distribution of permeable material in the interior. Under the assumption that the permeable material in the Moon is predominately free iron and iron-bearing minerals, the lunar iron abundance can be calculated from the lunar permeability for assumed compositional models of the interior. Since the amount of iron present in the lunar interior should be consistent with the measured global magnetic permeability, the permeability in effect places a constraint on the physical and chemical composition of the Moon's interior.

## GLOBAL MAGNETIC PERMEABILITY

Deployment of Apollo magnetometers on the lunar surface allowed simultaneous measurements of the external inducing field (by Explorer 25) and the total response field at the lunar surface (by an Apollo magnetometer). The total response field measured at the surface by an Apollo magnetometer is the sum of the external and induced fields:

$$\underline{B} = \mu \underline{H} = \underline{H} + 4\pi \underline{M} \quad (7)$$

where  $\underline{H}$  is the external magnetizing field and  $\underline{M}$  is the magnetization field induced in the permeable lunar material (see fig. 26). The relative magnetic permeability is  $\mu = 1 + 4\pi k$ , where  $k$  is magnetic susceptibility in emu/cm<sup>3</sup>. Since the dipolar magnetization  $\underline{M}$  is known to be below the Explorer 35 magnetometer resolution (ref. 8), it is assumed in the dual magnetometer analysis that Explorer 35 measures  $\underline{H}$  alone.

For the two-layer lunar permeability

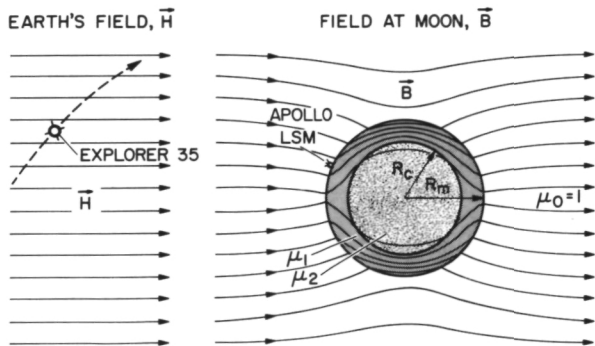


Figure 26.—Magnetization induction in the Moon.

When the Moon is immersed in a uniform external field  $\underline{H}$  (in this case the steady geomagnetic tail field), a dipolar magnetization field  $\underline{M}$  is induced in permeable material in the lunar interior, with the dipole axis of  $\underline{M}$  aligned along the direction of  $\underline{H}$ . The total magnetic field near the Moon is  $\underline{B} = \underline{H} + 4\pi \underline{M}$ . The magnetic permeabilities of the two layers are  $\mu_1$  and  $\mu_2$ , and for regions outside the Moon,  $\mu = \mu_0 = 1$  (free space).  $\underline{H}$  is measured by the lunar orbiting Explorer 35, whereas  $\underline{B}$  is measured by an Apollo lunar surface magnetometer (LSM). Measurements of  $\underline{B}$  and  $\underline{H}$  allow construction of a  $\underline{B}$ - $\underline{H}$  hysteresis curve for the sphere, from which permeability and iron abundance can be calculated.

model illustrated in figure 26 (which will be referred to later when iron abundance results are reviewed), the total field at the outer surface of the sphere is expressed

$$\underline{B} = H_x(1 + 2G)\hat{x} + H_y(1-G)\hat{y} + H_z(1-G)\hat{z} \quad (8)$$

where

$$G = \frac{(2\eta + 1)(\mu_1 - 1) - \lambda^3(\eta - 1)(2\mu_1 + 1)}{(2\eta + 1)(\mu_1 + 2) - 2\lambda^3(\eta - 1)(\mu_1 - 1)} \quad (9)$$

Here  $\eta = \mu_1/\mu_2$ ;  $\mu_1$  and  $\mu_2$  are relative permeability of the shell and core, respectively. The permeability exterior to the sphere is  $\mu_0 = 1$ , that of free space;  $\lambda = R_c/R_m$ ;  $R_c$  and  $R_m$  are radius of the core and the Moon, respectively. Equation (8) expresses the total surface field in a coordinate system which has its origin on the lunar surface at an Apollo magnetometer site:  $\hat{x}$  is directed radially outward from the lunar surface, and  $\hat{y}$  and  $\hat{z}$  are tangential to the surface, directed eastward and northward, respectively.

A plot of any component of equation (8) will result in a  $\underline{B}$ - $\underline{H}$  hysteresis curve. Equation (9) relates the slope of the hysteresis curve to the lunar permeability. The average whole-Moon permeability  $\mu$  is calculated from the hysteresis-curve slope by setting  $\mu_1 = \mu_2 = \mu$  in equation (9):

$$G = \frac{\mu - 1}{\mu + 2} \quad (10)$$

The hysteresis-curve method of permeability analysis was first employed by Dyal and Parkin (ref. 38) to calculate the whole-Moon permeability result  $1.03 \pm 0.13$ . Since then the error limits have been lowered by processing a larger number of simultaneous data sets and using more rigid data selection criteria (e.g., ref. 85).

In the most recent dual-magnetometer results (refs. 32 and 33), a hysteresis curve was constructed with 2703 data sets (see fig. 27). Since the external magnetizing field is so small ( $\sim 10$  gammas), the familiar "S" shape of the hysteresis curve degenerates to a straight line (ref. 86). The data were fit by a least-squares technique which yields the

slope best-estimate of  $1.008 \pm 0.004$ . By use of this value with the radial ( $x$ ) component of equation (8) and equation (10), the whole-Moon permeability was calculated to be  $\mu = 1.012 \pm 0.006$  ( $2\sigma$  error limits). Both extremes are greater than 1.0, implying that the Moon, as a whole, acts as a paramagnetic or weakly ferromagnetic sphere. This result has been used to calculate the iron abundance of the Moon as discussed in the next section.

Russell et al. (ref. 34) have recently made permeability calculations using data from a

single magnetometer, the Apollo 15 subsatellite magnetometer orbiting at an altitude about 100 km above the Moon. The results indicate that the relative permeability of the entire spherical volume enclosed by the satellite orbit is below 1.0, implying that the layer between the Moon and the satellite orbit is diamagnetic. The charged particles measured on the lunar surface by the Rice University suprathreshold ion detector experiments (ref. 87) may be from a lunar ionosphere. If an ionosphere fills the entire region between the lunar surface and the subsatellite at 100 km altitude, the interior global lunar permeability would be higher than that calculated under the assumption of no ionosphere. The lunar permeability value of Parkin et al. (ref. 32) would be adjusted upward from 1.012 to 1.017, provided there exists a lunar ionosphere compatible with the measurements of Russell et al. (ref. 34). The corresponding free iron abundance value would be 3.9 instead of 2.5 wt.%. The existence of a lunar ionosphere is uncertain at present; further investigation is required, using both magnetic and plasma data.

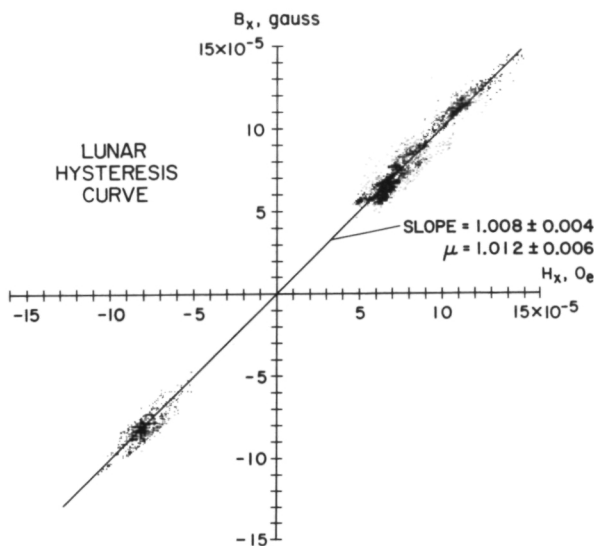


Figure 27.—Hysteresis curve for the Moon. Data points are 2703 simultaneous 2-minute averages of radial components of the external geomagnetic field data  $H$  (measured by the lunar orbiting Explorer 35 Ames magnetometer) and total magnetic induction  $B = \mu H$  ( $B$  is measured by the Apollo 12 lunar surface magnetometer). Data points are selected from four lunations of measurements made when the Moon is immersed in the uniform geomagnetic tail field, far from the neutral sheet in the tail. In this low-external-field regime ( $\sim 10$  gammas or  $10^{-4}$  Oe), the hysteresis curve is linear and is fitted by a least-squares line of slope  $1.008 \pm 0.004$ . This slope corresponds to a whole-Moon magnetic permeability of  $1.012 \pm 0.006$ . The least-squares line intersects the origin exactly in this figure because the vertical-axis intercept (the radial or  $x$ -component of the remanent field at the Apollo 12 site) was subtracted out after the least-squares fit was made.

## LUNAR IRON ABUNDANCE

Iron abundance calculations have been presented by various authors, in theoretical treatments based on geochemical and geophysical properties calculated for bodies of planetary size (refs. 88, 89, and 90) or on measured compositions of meteorites (ref. 91). Recently Parkin et al. (refs. 32, 33, and 85) have used a global lunar permeability measurement, determined from magnetic field measurements, to calculate lunar iron abundance for the Moon. In their calculations the Moon is modeled by a homogeneous paramagnetic rock matrix (olivine and orthopyroxene models are used), in which free metallic iron is uniformly distributed. Pyroxenes and olivines have been reported to be major mineral components of the lunar surface fines and rock samples (refs. 18, 92, and 93), with combined iron present as the paramagnetic  $Fe^{2+}$  ion. The ferromagnetic

component of lunar samples is primarily metallic iron which is sometimes alloyed with small amounts of nickel and cobalt (refs. 17 and 19). This free iron is thought to be native to the Moon (because of its low nickel content) rather than meteoritic in origin (ref. 71). Orthopyroxene and olivine models are consistent with geochemical studies (refs. 94–97) and geophysical studies (ref. 98).

Since the susceptibility of free iron changes several orders of magnitude at the iron Curie temperature ( $T_c$ ), Parkin et al. have used a two-layer model with the core-shell boundary  $R_c$  at the Curie isotherm (see fig. 26). For  $R > R_c$ ,  $T < T_c$ , and for  $R \leq R_c$ ,  $T > T_c$ . Therefore, for  $R > R_c$  any free iron is ferromagnetic while at greater depths where  $T > T_c$ , the free iron is paramagnetic. The Curie isotherm location is determined from the thermal profile used for a particular model. Three thermal models have been used in the calculations. For model profile  $T_1$  the Curie isotherm is spherically symmetric and located at  $R_c/R_m = 0.9$ . Shell and core temperatures are  $600^\circ\text{C}$  and  $1400^\circ\text{C}$ , respectively. For the model profile  $T_2$  the shell is  $500^\circ\text{C}$  and the core is  $1300^\circ\text{C}$ , while the Curie isotherm boundary is at  $R_c/R_m = 0.85$ . Temperatures are  $300^\circ\text{C}$  and  $700^\circ\text{C}$  for shell and core of model profile  $T_3$ , which has  $R_c/R_m = 0.7$ . In the outer shell there are both ferromagnetic and paramagnetic contributions to the total magnetic permeability  $\mu_1 = 1 + 4\pi k_1$ . The susceptibility of the shell is  $k_1 = k_{1c} + k_{1a}$ , where  $k_{1a}$  is "apparent" ferromagnetic susceptibility and  $k_{1c}$  is paramagnetic susceptibility. The ferromagnetic component is metallic free iron, assumed to be composed of multidomain, noninteracting grains; the paramagnetic component is  $\text{Fe}^{2+}$  combined in the orthopyroxene or olivine rock matrix. The measured ferromagnetic susceptibility of the shell material is an apparent value which differs from the intrinsic ferromagnetic susceptibility of the iron because of self-demagnetization of the iron grains and the volume fraction of iron in the shell. For  $R < R_c$  the lunar material is paramagnetic only, with susceptibility  $k_2$

$= k_{2c} + k_{2a}$ ;  $k_{2c}$  is the contribution of paramagnetic chemically combined iron, and  $k_{2a}$  is the apparent susceptibility of free paramagnetic iron above the Curie temperature.

Using the information described in the previous paragraphs, Parkin et al. (ref. 33) have generated the curves shown in figure 28, which relate free iron abundance ( $q$ ) and total iron abundance ( $Q$ ) to the hysteresis-curve slope. The results are summarized in table 3 and figure 29. The *minimum* total iron abundance consistent with the hysteresis curve can be calculated assuming the whole-Moon permeability corresponds

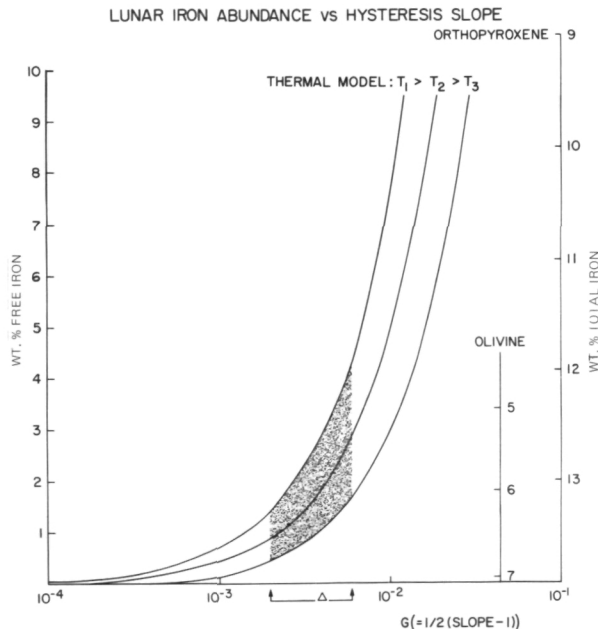


Figure 28.—Iron abundance in the Moon as a function of global hysteresis curve slope. Free iron abundance ( $q$ ) and total iron abundance ( $Q$ ) versus the parameter  $G$  (hysteresis curve slope equals  $2G + 1$ ) for three temperature profiles described in the text. Total iron abundance is shown for two lunar composition models, orthopyroxene and olivine. Arrows below the horizontal axis show the range of the parameter  $G$ , experimentally determined from the hysteresis curve slope:  $G = 0.004 \pm 0.002$ . The shaded region defines the allowed values of free and total iron abundances, bounded by hysteresis curve error limits and by thermal models  $T_1$  and  $T_3$ .

Table 3.—Iron Abundance of the Moon as a Function of Thermal and Compositional Models

		Free Iron Abundance, weight percent			Total Iron Abundance, weight percent		
		T <sub>3</sub>	T <sub>2</sub>	T <sub>1</sub>	T <sub>3</sub>	T <sub>2</sub>	T <sub>1</sub>
Compositional Model	Thermal Model						
	Orthopyroxene	1.0 ± 0.5	2.0 ± 1.0	3.0 ± 1.5	13.4 ± 0.3	13.0 ± 0.5	12.6 ± 0.6
	Olivine	1.0 ± 0.5	2.0 ± 1.0	3.0 ± 1.5	6.5 ± 0.3	5.9 ± 0.7	5.3 ± 1.0

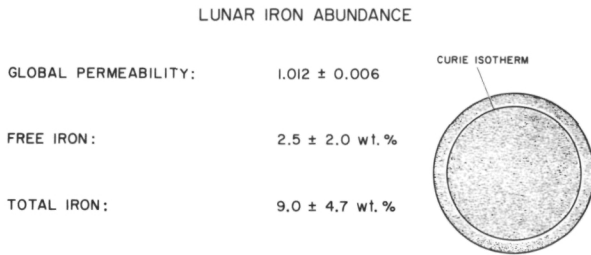


Figure 29.—Summary of global lunar magnetic permeability, free iron abundance, and total iron abundance.

entirely to ferromagnetic iron in the outer shell where the temperature is below the Curie point. For this case the bulk iron abundance is 0.9 + 0.5 wt.%. It is noted that the susceptibilities of both olivine and pyroxene are about an order of magnitude too small to account for the measured permeability without some ferromagnetic material present.

**CONSIDERATIONS OF AN IRON CORE AND IRON-RICH LAYER**

The whole-Moon permeability has also been used by Parkin et al. (ref. 32) to investigate the magnetic effects of a hypothetical iron core in the Moon. Density and moment of inertia measurements for the Moon limit the size of such a core to less

than 500 km in radius (ref. 98). If this hypothetical iron core were entirely paramagnetic and the surrounding core were orthopyroxene of average temperature 1100° C the global permeability would be 1.0003. This value is small compared with the measured permeability of 1.012 ± 0.006, implying that if such a small paramagnetic iron core exists, its magnetization is masked by magnetic material lying nearer to the surface. Therefore, the hysteresis measurements can neither confirm nor rule out the existence of a small iron core in the Moon.

An iron-rich layer in the Moon has been considered by several investigators (refs. 94, 95, and 99). It is possible that early melting and subsequent differentiation of the outer several hundred kilometers of the Moon may have resulted in the formation of a high-density, iron-rich layer beneath a low-density, iron-depleted crust. Constraints have been placed on an iron-rich layer by Gast and Giuli (ref. 99) using geochemical and geophysical data (for example, measurements of lunar moments of inertia). One set of their models consists of high-density layers between depths of 100 km and 300 km. At a depth of 100 km the allowed layer thickness is 12 km; the thickness increases with increasing depth, to 50 km at 300-km depth. Also presented is a set of layers at 500-km depth. Using exactly the same considerations as were used in the iron abundance calculations, Parkin et al. have

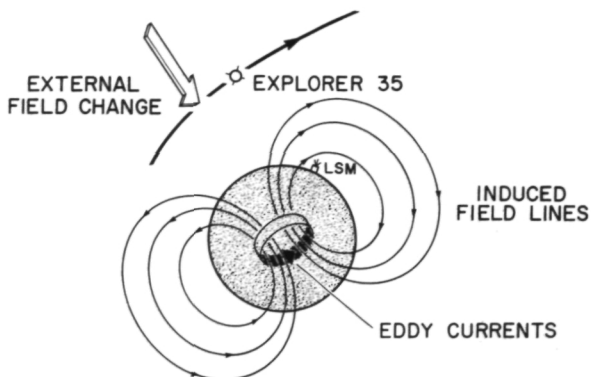


Figure 30.—Global eddy-current induction: Moon in the geomagnetic tail. The induced poloidal field experiences greatly reduced plasma effects, especially in deep-lobe regions of the tail far from the neutral sheet. The poloidal field is considered to be an unconfined (vacuum) dipole field for analytical purposes.

calculated whole-Moon permeabilities which would be expected from lunar models with these iron-rich layers. The calculations indicate that all iron-rich layers allowed by geophysical constraints as outlined by Gast and Giuli, if wholly above the iron Curie temperature, would yield global permeabilities of about 1.00006. As for the case of a small lunar iron core, the magnetization field of such paramagnetic layers would be masked by ferromagnetic materials elsewhere in the Moon, and the hysteresis curve measurements can neither confirm nor rule out these layers. This conclusion would particularly apply to the Gast-Giuli layers at 500-km depths, which are almost certainly paramagnetic. If the iron-rich layers are below the Curie temperature and therefore ferromagnetic, they yield global permeabilities of about 3.5. This is above the upper limit for the measured permeability of  $1.012 \pm 0.006$  and the Gast-Giuli layers can be ruled out if they are cool enough to be ferromagnetic. It is important to realize that the high-density layers discussed by Gast and Giuli (ref. 99) can be thought of as limiting cases and that there are innumerable less dense and thinner layers which are allowed by geophysical, geochemical, and magnetic constraints.

## Global Eddy-Current Induction: Electrical Conductivity and Temperature

Electrical conductivity and temperature of the Moon have been calculated from global eddy-current response to changes in the magnetic field external to the Moon. When the Moon is subjected to a change in the external field, an eddy-current field is induced in the Moon which opposes the change (see fig. 30). The induced field responds with a time dependence which is a function of the electrical conductivity distribution in the lunar interior. Simultaneous measurements of the transient driving field (by Explorer 35) and the lunar response field (by an Apollo surface magnetometer) allow calculation of the lunar conductivity. Since conductivity is related to temperature, a temperature profile can be calculated for an assumed compositional model of the lunar interior.

When the Moon is in the solar wind, lunar

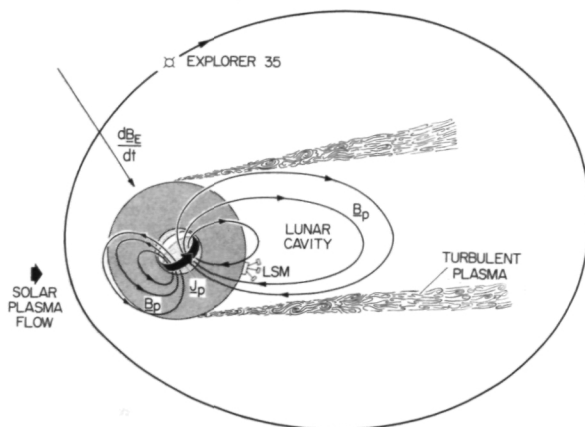


Figure 31.—Global eddy-current induction: Moon in the solar wind. Eddy currents and corresponding poloidal magnetic fields are induced by response to time-dependent fluctuations in the external field  $B_E$ . The poloidal field has different characteristics, depending on the Moon's environment. When the Moon is in the solar wind, the global induced field is asymmetrically confined by the solar wind flowing past the Moon; the field is compressed on the day (sunlit) side and confined to the cavity region on the night (antisolar) side of the Moon.

eddy-current fields form an induced lunar magnetosphere which is distorted in a complex manner due to flow of solar wind plasma past the Moon. The eddy-current field is compressed on the dayside of the Moon and is swept downstream and confined to the "cavity" on the lunar nightside (see fig. 31). Because of the complexity, early analysis included a theory for transient response of a sphere in a vacuum in order to model lunar response as measured on the lunar nightside (refs. 43, 44, and 100). The transient technique has subsequently been further developed to include effects of cavity confinement on nightside tangential data and to introduce analysis of magnetic step transients measured on the lunar dayside (refs. 45 and 51). Recently time-dependent poloidal response of

a sphere in a vacuum has been applied to data measured in the geomagnetic tail (refs. 72 and 101) where plasma confinement effects are minimized. The poloidal response analysis has been used to determine the electrical conductivity and temperature profiles of the lunar interior.

ELECTRICAL CONDUCTIVITY ANALYSIS: MOON IN SOLAR WIND PLASMA

Lunar Nightside Data Analysis

The lunar electrical conductivity has been investigated by analysis of the lunar response to transients in the solar wind magnetic field. The response, measured by an Apollo

NIGHTTIME TRANSIENT RESPONSE

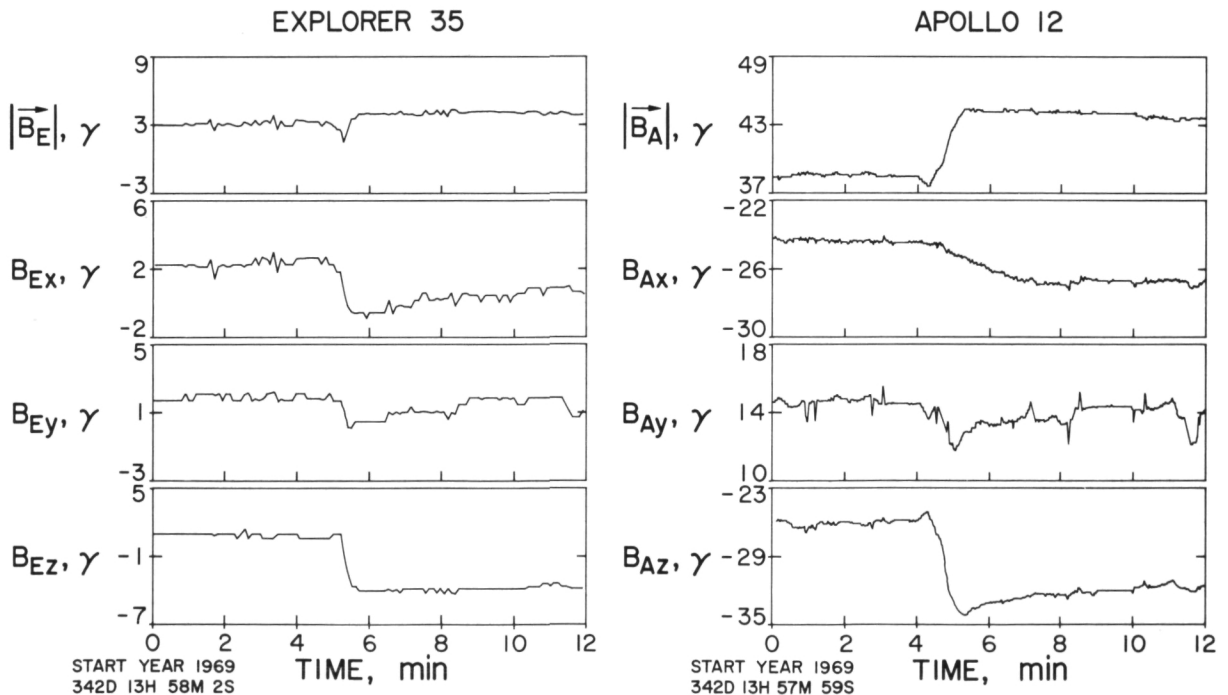


Figure 32.—Nighttime transient response magnetic field data. A transient measured by an Apollo LSM while on the nighttime (antisolar) side of the Moon, showing simultaneous external solar wind field data measured by Explorer 35. Data are expressed in the surface coordinate system which has its origin at the Apollo 12 magnetometer site;  $\hat{x}$  is directed radially outward from the surface, while  $\hat{y}$  and  $\hat{z}$  are tangent to the surface, directed eastward and northward, respectively.

magnetometer on the nightside of the Moon, is theoretically approximated by the response of a conducting sphere in a vacuum. The theory has been developed by extending the work of Smythe (ref. 39) and Wait (ref. 40) for a radially varying lunar conductivity profile (ref. 102). Figure 32 shows an example of an event in which a transient in the external solar wind magnetic field is measured simultaneously by the Explorer 35 Ames magnetometer and an Apollo surface magnetometer. The transient is essentially a rotation in the external field, as indicated by the near-constancy of the field magnitude  $|\underline{B}_E|$  measured by Explorer 35. Simultaneous field data ( $\underline{B}_A$ ), measured on the nightside of the Moon by the Apollo 12 lunar surface magnetometer, are the vector sum of the external driving field  $\underline{B}_E$ , the induced eddy-current poloidal field  $\underline{B}_P$ , and the constant remanent field  $\underline{B}_R$  (see equation (4)). Again,

the field components are expressed in a coordinate system which has its origin located at the Apollo LSM site on the lunar surface;  $\hat{x}$  is directed radially outward from the Moon, and  $\hat{y}$  and  $\hat{z}$  are tangential to the lunar surface, directed eastward and northward, respectively.

Figure 33 shows averages of radial components of the measured response field ( $B_{Ax}$ ) for eleven normalized transient events of the type illustrated in figure 32. Error bars are standard deviations of the measured responses.

For models of the interior of the Moon a family of conductivity profiles (all of which monotonically increase with depth in the Moon), the theoretical response to a fast ramp is calculated and compared with the measured response. For this analysis the external field transient is represented by a ramp input function which falls from unity

## NIGHTSIDE DATA

## DAYSIDE DATA

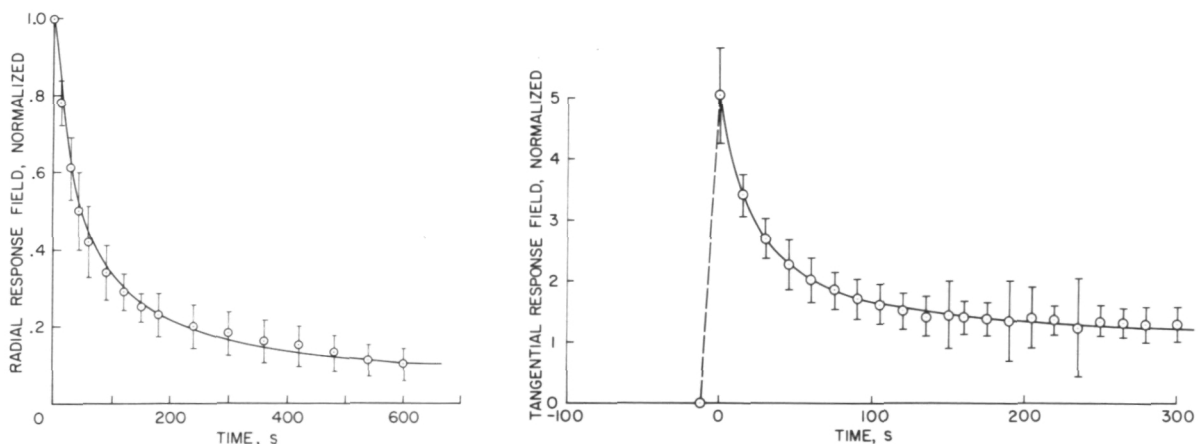


Figure 33.—Normalized averages of transient response data, measured when Moon was in the solar wind. (a) Nightside transient response data, showing decay characteristics of the radial component of the total surface field  $B_{Ax}$  after arrival of a step transient which reduces the external magnetic field radial component by an amount  $\Delta B_{Ex}$ , here normalized to one. The shape of the curve illustrates time characteristics of the decay of the induced poloidal eddy-current field. (b) Daytime transient response data, showing decay characteristics of tangential components ( $B_{Ay,z}$ ) of the total surface field after arrival of a step transient which increases the external magnetic field tangential component by an amount  $\Delta B_{Ey,z}$ , here normalized to one. Shape of the curve again illustrates decay characteristics of the induced poloidal field. The overshoot maximum is amplified to  $\sim 5$  by solar wind dayside compression; the theoretical overshoot maximum is 1.5 for an unconfined poloidal field.

to zero in 15 seconds, a time characterizing convection of a solar wind discontinuity past the Moon. (For a 400 km/s solar wind, this time is 10–20 seconds, depending on the thickness of the discontinuity and the inclination of its normal to the solar wind velocity.) The input field is constant before and after the field change. A particular set of

conductivity profiles yield response functions which pass within all data error bars of figure 33. These profiles define the shaded region of figure 34 and are all consistent with the nightside response data.

### Lunar Dayside Data Analysis

Induced lunar eddy-current fields are confined, by the highly conducting solar wind, to the inside of the Moon and a small region above the lunar surface on the lunar dayside and to a "cavity" region on the nightside. Due to the complexity of the confinement, the conductivity analysis of transient magnetometer data measured on the lunar dayside has involved modeling the Moon by a sphere of homogeneous conductivity; the induced eddy-current field  $B_p$  is considered to be totally confined inside the lunar sphere (ref. 45). Figure 35 shows an example of a transient event in the solar wind magnetic field which is measured on the lunar dayside. Figure 33 shows averages of tangential components of response fields, measured on the lunar dayside, induced in response to rising fast-ramp transients in the free-streaming solar wind (error bars are standard deviations). The overshoot maximum is amplified by a factor of 5 over the external input field step change, by solar wind dayside confinement of the surface tangential field components. The data are fit by a lunar conductivity model with a homogeneous core of radius  $R_c = 0.9 R_m$  and conductivity  $\sigma \sim 10^{-3}$  mhos/m. This result is consistent with the nightside conductivity profile illustrated in figure 34 to depths allowed by the duration of the response data which is shown in figure 33.

The theoretical models outlined so far have all assumed spherical symmetry to describe lunar eddy-current response to changes in the external field. However, the nightside and dayside analyses have used data taken when the Moon was immersed in the solar wind plasma with asymmetric confinement of the inducing fields. The shortcomings of using spherically symmetric approximations to describe the induced lunar magnetosphere,

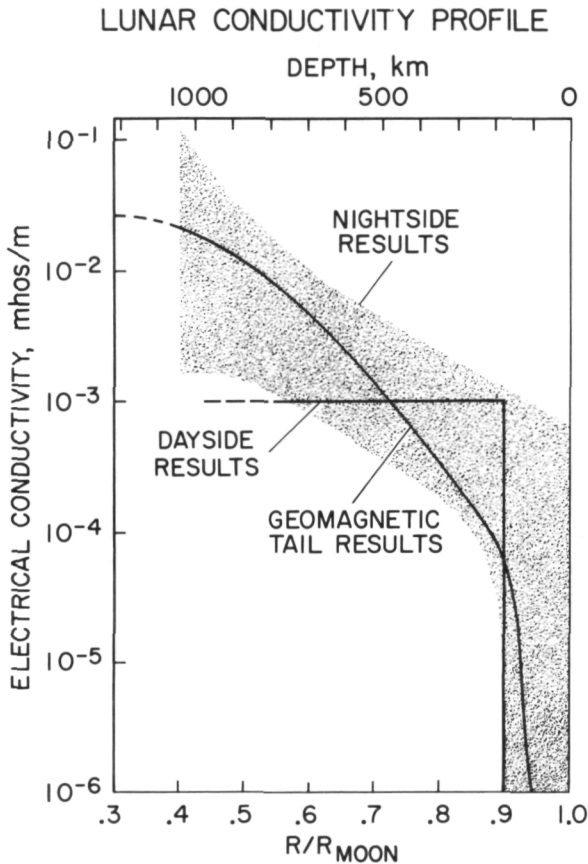


Figure 34.—Electrical conductivity profiles for the lunar interior calculated from measurements in different regions of the lunar orbit around the Earth. The shaded region is from analysis of nightside transient data averages shown in figure 33 (a). The dayside conductivity profile is calculated by fitting totally confined two-layer Moon models to the dayside tangential component data illustrated in figure 33 (b). The curve labeled "geomagnetic tail results" is a profile consistent with analysis of transients in the geomagnetic tail lobes such as events illustrated in figures 37 and 39. Errors associated with this latter curve are approximately the same as the conductivity band shown for the nightside results.

## DAYTIME TRANSIENT RESPONSE

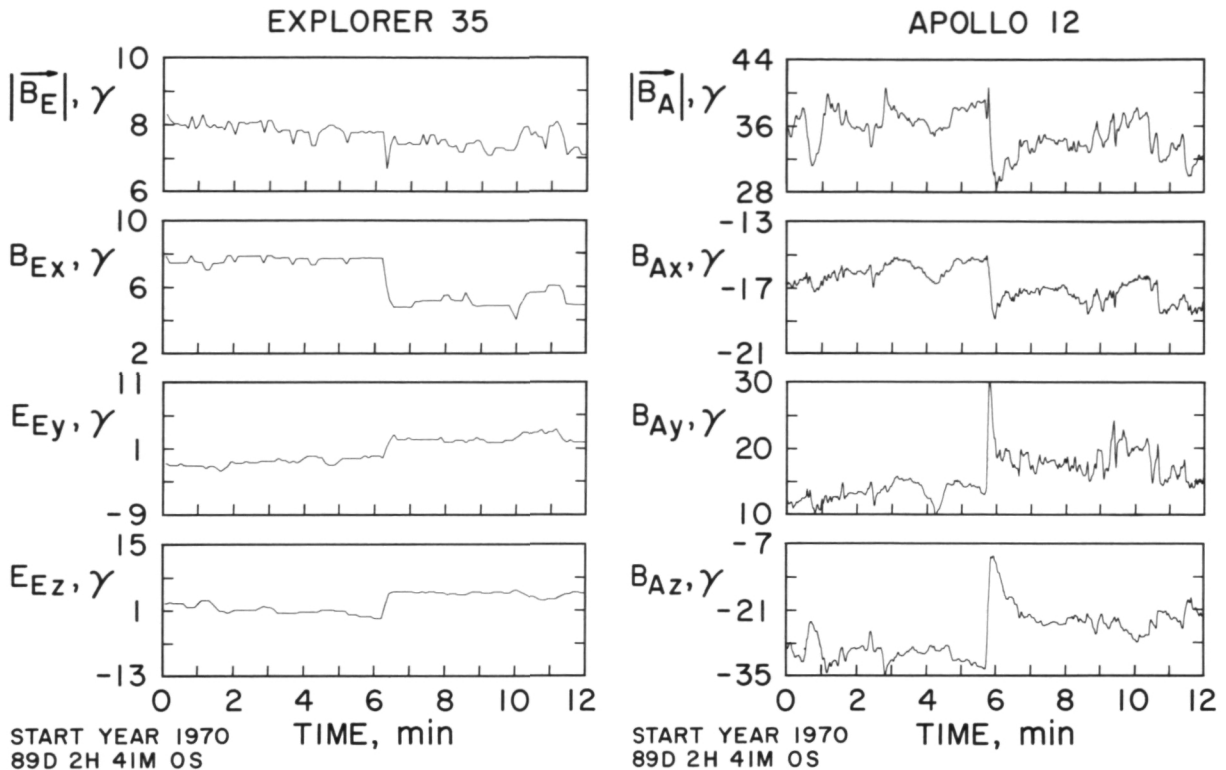


Figure 35.—Daytime transient response magnetic field data, measured by an Apollo LSM while on the day-side (subsolar side) of the Moon, showing simultaneous external solar wind field data measured by lunar orbiting Explorer 35. The coordinate system is defined in the text. Note in particular the tangential components: dayside overshoot amplification is much higher relative to the Explorer-measured external step magnitudes than is nighttime amplification (shown in fig. 32).

which is actually asymmetrically confined, have been pointed out in the literature for both the nightside vacuum approximation (see, e.g., ref. 52) and the dayside totally confined approximation (see e.g. ref. 51). Three-dimensional, dynamic asymmetric confinement presents a difficult theoretical problem which has not been solved at the time of this writing. Previous theoretical approximations of the asymmetric problem have included a two-dimensional approximation (ref. 50); three-dimensional static theory for a point-dipole source, with substantiating laboratory data (ref. 51); a three-dimensional dynamic theory for particular orientations of variations in the external field (ref. 103).

The confinement of the induced poloidal field by the highly conducting solar wind has been studied in the laboratory by considering a point-dipole field inside a superconducting cylinder (ref. 51). Two geometrical orientations of the point dipole have been considered: along the cylinder axis, and transverse to the cylinder axis. (See inserts in figure 36 for an illustration of these orientations.) The fields of the dipole-oriented transverse and axial with respect to the cylinder axis have been determined following Parker (ref. 104) and P. Cassen (private communication). The highly conducting solar wind plasma cavity is modeled by a thin lead superconducting capped cylinder and the instantaneous induced poloidal field is modeled by a small

dipolar samarium-cobalt magnet placed equidistant from the closed end and the side walls of the cylinder. The measured ratios of confined fields to unconfined fields are shown in figure 36. The theory and laboratory data presented in figure 36 represent to first order the effects of solar wind compression on a poloidal induced lunar field, as measured by a lunar surface magnetometer positioned at the antisolar point.

sion, plasma diamagnetism, etc.) are minimal.

### Poloidal Response of a Sphere in a Vacuum: Theory

In the conductivity profile analysis we assume that plasma effects are negligible in the lobe regions of the geomagnetic tail, and that the response of the Moon can be represented as that of a conducting sphere in a vacuum. To describe the response of a lunar sphere to an arbitrary input field in the geomagnetic tail, we define the magnetic vector potential  $\underline{A}$  such that  $\nabla \times \underline{A} = \underline{B}$  and  $\nabla \cdot \underline{A} = 0$ . We seek the response to an input  $\underline{\Delta B}_E b(t)$ , where  $b(t) = 0$  for  $t < 0$  and  $b(t)$  approaches unity as  $t \rightarrow \infty$ . The direction of  $\underline{\Delta B}_E$  is taken to be the axis of a spherical coordinate system  $(r, \theta, \phi)$ . If the conductivity is spherically symmetric, the transient magnetic field response has no  $\phi$  component,

### ELECTRICAL CONDUCTIVITY ANALYSIS: MOON IN THE GEOMAGNETIC TAIL

In order to circumvent the problem of asymmetry, recent analyses (refs. 72 and 101) have considered lunar eddy-current response during times when the Moon is in the geomagnetic tail where plasma interaction effects encountered in the solar wind (asymmetric confinement, remanent field compres-

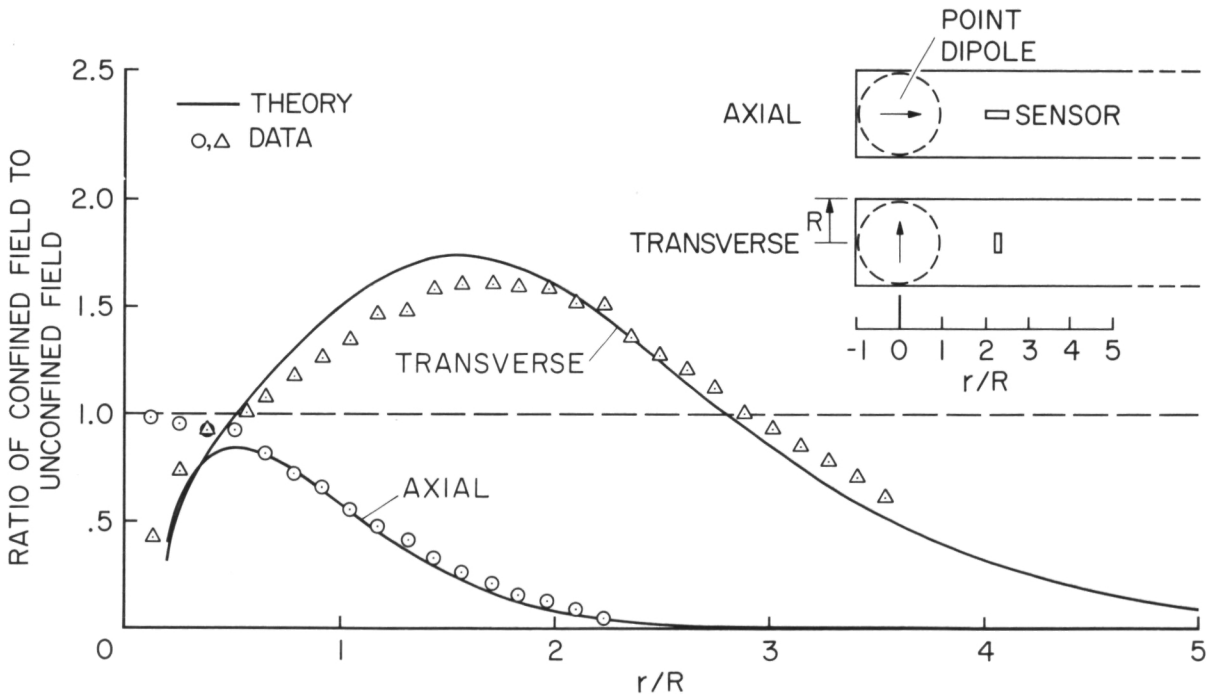


Figure 36.—Confinement of a point dipole magnetic field, shown theoretically and experimentally. The inserts schematically show lunar confinement by the solar wind, approximated by a capped-cylinder superconductor enclosing a point dipole field. The theoretical curves show ratios of a confined to an unconfined dipolar field versus distance along the cylinder axis. Data are results of a laboratory experiment in which confinement of a small dipole magnet's field by a cylindrical superconductor is measured experimentally.

and hence  $\underline{A} = A\hat{e}_\phi$  and  $\partial/\partial \phi = 0$ . Under these conditions (and neglecting displacement currents) the laws of Faraday, Ampere, and Ohm combine to yield a diffusion equation (ref. 102) for the magnetic potential (in MKS units):

$$\Delta^2 \underline{A}(r, \theta; t) = \mu \sigma(r) \frac{\partial \underline{A}}{\partial t}(r, \theta; t) \quad (11)$$

From magnetization induction analysis it is shown that  $\mu \cong \mu_0$ , that of free space (ref. 32). Then, for  $t > 0$ , the magnetic field must be continuous at the surface, so that  $\underline{A}$  and  $\partial \underline{A}/\partial r$  must always be continuous at  $r = R_m$ , the radius of the sphere. We also have the boundary condition  $\underline{A}(0, t) = 0$  and the initial condition  $\underline{A}(r, \theta, \phi) = 0$  inside the Moon. Outside the Moon, where  $\sigma = 0$ ,

$$A = \Delta B_E \left( \frac{r}{2} \right) b(t) \sin \theta + \frac{\Delta B_E}{r^2} f(t) \sin \theta. \quad (12)$$

The first term on the right is a uniform magnetic field modulated by  $b(t)$ ; the second term is the (as yet unknown) external transient response, which must vanish as  $r \rightarrow \infty$ , and  $t \rightarrow \infty$ . Note that at  $r = R_m$  where  $R_m$  is normalized to unity,

$$A = \Delta B_E \sin \theta \left( \frac{b(t)}{2} + f(t) \right) \quad (13)$$

and

$$\frac{\partial A}{\partial r} = \Delta B_E \sin \theta \left( \frac{b(t)}{2} - 2f(t) \right). \quad (14)$$

Therefore, at  $r = R_m = 1$ ,

$$\frac{\partial A}{\partial r} = -2A + \frac{3}{2} \left( \Delta B_E \sin \theta b(t) \right). \quad (15)$$

Since the magnetic field is continuous at  $r = r_m$ , this is a boundary condition for the interior problem. Letting  $G(r, t) = A / \Delta B_E \sin \theta$  and  $\bar{G}(r, s)$  be the Laplace transform

### GEOMAGNETIC TAIL TRANSIENT RESPONSE

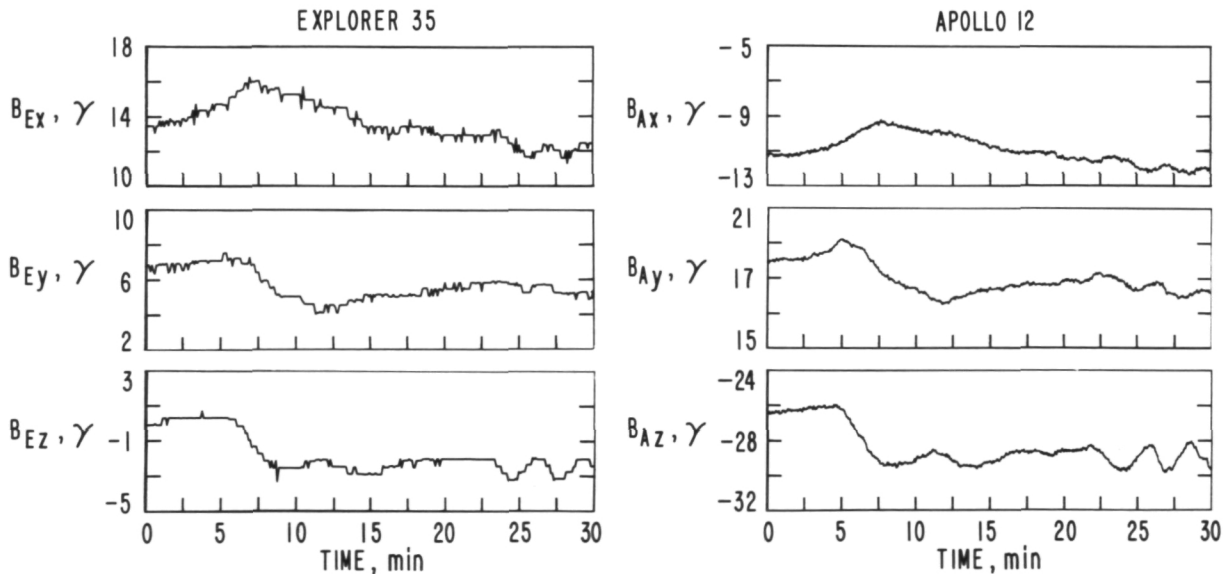


Figure 37.—Magnetic transient event measured simultaneously by the Apollo 12 LSM and the Explorer 35 Ames magnetometer deep in the north lobe of the geomagnetic tail. Data are expressed in the surface coordinate system which has its origin at the Apollo 12 magnetometer site;  $x$  is directed radially outward from the surface, while  $y$  and  $z$  are tangent to the surface, directed eastward and northward, respectively. Due to poloidal field induction in the Moon, the Apollo 12 radial ( $\hat{x}$ ) component is "damped" relative to the Explorer 35 radial component, whereas the Apollo 12 tangential ( $\hat{y}$  and  $\hat{z}$ ) field components are "amplified" relative to Explorer 35 data.

of  $G$ , equation (1) becomes

$$\frac{1}{r} \left( \frac{\partial^2}{\partial r^2} (r\bar{G}) - \frac{2}{r} \bar{G} \right) = s\mu_0\sigma(r)\bar{G} \quad (16)$$

for the interior. The boundary conditions are

$$\frac{\partial \bar{G}}{\partial r} = -2\bar{G} + \frac{3}{2}\bar{b}(s) \quad (17)$$

$$\text{at } r = R_m \text{ and } \bar{G} = 0 \quad (18)$$

at  $r = 0$ .

Since the governing equations are linear, the response to a general time-dependent input function can be found by superposition of solutions as follows. The individual input function (that is, external field transient event measured by Explorer 35) is approximated by a succession of ramp functions  $b_i(t)$ . For each  $b_i(t)$  and the given conductivity profile  $\sigma(r)$ , the above system of equations is numerically integrated to obtain  $\bar{G}_i(r,s)$  in the range  $0.2 \leq r \leq R_m$ . The function  $\bar{G}_i(r,s)$  is then numerically inverse Laplace transformed to find the characteristic transient response  $f_i(t)$  for the system. Then the individual functions  $f_i(t)$  are superposed to calculate the final time response function  $F(t)$  corresponding to the arbitrary input function and  $\sigma(r)$ . This calculated time series response is compared with the measured time series response (Apollo magnetometer data) and iterated with a different function  $\sigma(r)$  until the error between the calculated  $F(t)$  and the measured  $F(t)$  is minimized.

### Conductivity Results: Geomagnetic Tail Data Analysis

Figure 37 shows an example of a magnetic transient measured in the northward lobe of the geomagnetic tail. The data components are expressed in a coordinate system which has its origin on the lunar surface at the Apollo 12 magnetometer site. Again the x-component is directed radially outward from the lunar surface, while the y- and z-components are tangent to the surface, directed eastward and northward, respectively. The

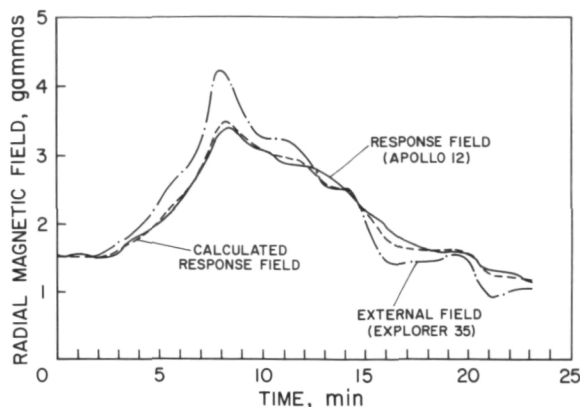


Figure 38.—*Electrical conductivity analysis for a transient event in the geomagnetic tail, deep in the north lobe. Shown are data from the radial component of the event of figure 37. Response to the Explorer 35 external field radial component is computed numerically for the conductivity profile shown in the insert of figure 40 and compared to the measured Apollo 12 response field. In the preliminary results of geomagnetic tail conductivity analysis, this selected conductivity profile, though not unique, yields a satisfactory fit of input and response data for this and thirteen other deep lobe tail events processed to date.*

external (terrestrial) driving magnetic field is measured by Explorer 35, whereas the total response field is measured on the lunar surface by the Apollo 12 magnetometer.

Figure 38 shows an example of calculated response for the Explorer 35 x-axis (radial) input function of figure 37, using the geomagnetic tail electrical conductivity profile illustrated in figure 34. Superimposed is the actual response which is the Apollo 12 x-component of figure 37. This conductivity profile yields the best fit of eighty profiles which have been run to date, although it is not unique. The profile also yields theoretical responses which fit well for the measured tangential components of figure 37 and the components of fourteen other deep-lobe geomagnetic tail transients which have been processed to date.

Figure 39 illustrates an example of a neutral sheet crossing. Figure 40 shows analysis of the radial components of the magnetometer measurements, using the conductivity profile determined from deep-lobe measurements. A

GEOMAGNETIC TAIL TRANSIENT RESPONSE

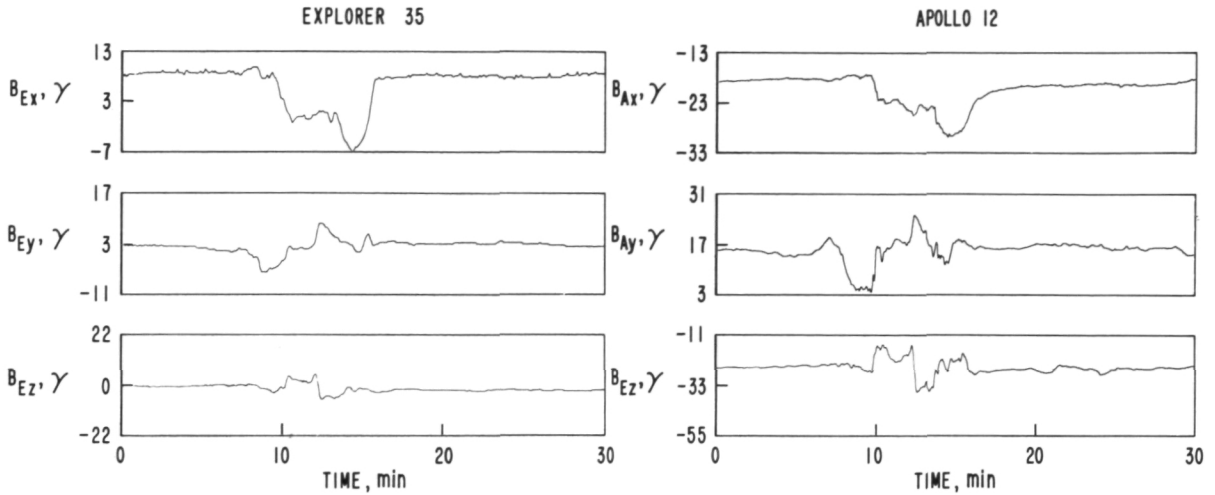


Figure 39.—Another transient event, measured in the plasma sheet of the geomagnetic tail. Details concerning the data are given in the figure 37 caption.

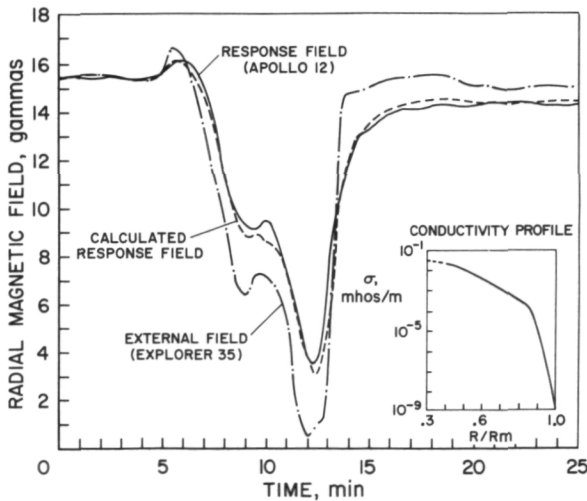


Figure 40.—Electrical conductivity analysis for the transient event measured in the plasma sheet of the geomagnetic tail. Shown are data from the radial component of the event of figure 39. Response to the Explorer 35 external field radial component is computed numerically for the conductivity profile shown in the insert and compared with the measured Apollo 12 response field.

qualitative fit of the data can be seen. It is surprising that these few selected neutral sheet data events are in such good agreement

with the deep-lobe events. An explanation of this will require further analysis.

Figure 34 shows a plot of the conductivity profile derived from deep-lobe geomagnetic field transient events, superimposed on the conductivity profiles derived from nightside transient-response data in the solar wind (ref. 45). The results are in general agreement. The geomagnetic tail conductivity profile is not unique; rather, it is one of a family of profiles, which results from the geomagnetic tail transient response analysis. The range of profiles from the geomagnetic tail analysis is approximately that of the nightside analysis shown by the shaded region in figure 34. In the future many more geomagnetic transient events will be processed to determine a range of conductivity profiles consistent with a large data set.

LUNAR TEMPERATURE PROFILES FROM CONDUCTIVITY ANALYSES

From an electrical conductivity profile the internal temperature distribution of the Moon can be inferred for an assumed lunar material composition (ref. 105). Electrical conduc-

tivity measurements are particularly useful for determination of lunar temperature because of the strong dependence of conductivity on the temperature of geological materials. The conductivity  $\sigma$  and temperature  $T$  of geological materials can be described by an equation of the form

$$\sigma = \sum_i E_i \exp(-a_i/kT) \quad (19)$$

where  $a_i$  represents the activation energies of impurity, intrinsic, and ionic conduction modes;  $E_i$  indicates material-dependent, temperature-independent constants; and  $k$  is Boltzmann's constant. Laboratory analyses relating conductivity to temperature for various minerals which are good geochemical candidates for the lunar interior, have been conducted by many investigators (e.g., refs. 106–110). These laboratory investigations have been designed to determine  $a_i$  and  $E_i$  of equation (19) and effects on these constants produced by the physical and chemical state of minerals. Duba (ref. 108) measured the conductivity of single olivine crystals as a function of temperature, pressure, and fayalite content. He concluded that conductivity was highly dependent on the oxidation state of the iron at temperatures below 1100° C. Later Duba and Nicholls (ref. 111) reported that the conductivity of a single olivine crystal under an oxygen fugacity of  $10^{-12}$  atm was almost three orders of magnitude lower than its conductivity measured in air. This decrease was attributed to the reduction of  $\text{Fe}^{3+}$  to  $\text{Fe}^{2+}$  in the sample. Duba et al. (ref. 110) measured the conductivity of olivine as a function of temperature up to 1440° C under controlled oxygen fugacity and found the measurements to be essentially pressure independent (up to 8 kbars). These recent measurements for olivine by Duba et al. were used to convert conductivity profiles in figure 34 labeled nightside results and geomagnetic tail results, respectively, to temperature profiles numbered 1 and 2 in figure 41. Also included in figure 41, for comparison, are profiles resulting from thermal history calculations of two other investigators. One must be aware that large uncertainties in the lunar temperature

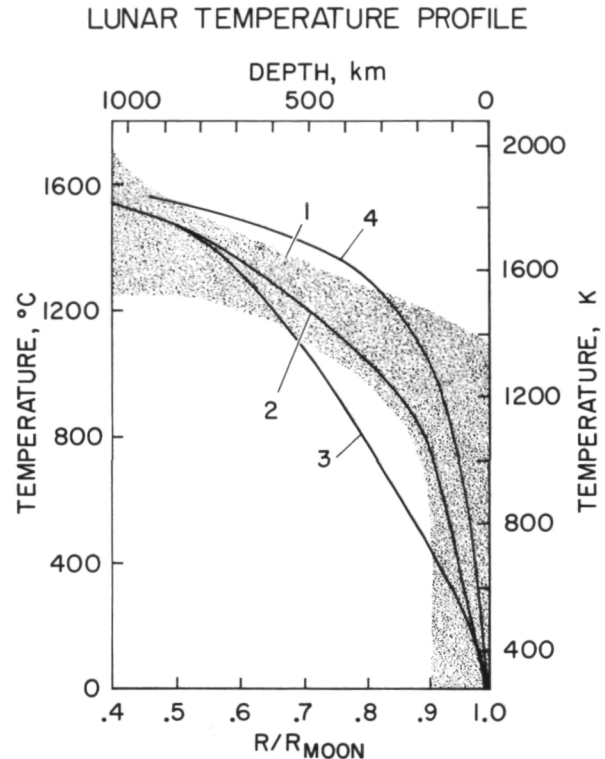


Figure 41.—Comparison of lunar temperature profiles calculated by different investigators. 1: Temperature profile calculated from the "nightside" conductivity profile shown in figure 34, by use of laboratory data relating conductivity to temperature for olivine (ref. 110). 2: Profile calculated from the "geomagnetic tail" conductivity profile of figure 26 and the data from Duba et al. (ref. 110). 3,4: Temperature profiles from thermal history calculations of Toksöz (ref. 98) and Hanks and Anderson (ref. 119).

profile will remain until more definitive laboratory and space measurements are completed.

## Measurements of the Magnetopause and Bow Shock

With the use of simultaneous data from magnetometers on the lunar surface and in orbit around the Moon, the velocity and thickness of the Earth's magnetopause and bow shock (see fig. 42) have been measured at the lunar orbit. The boundary crossings are measured simultaneously by the Apollo 12

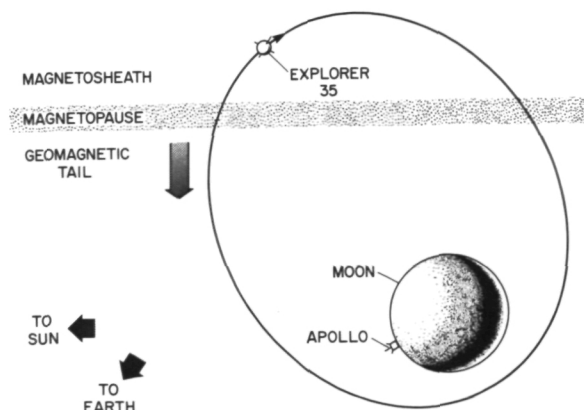


Figure 42.—Schematic diagram depicting a crossing of the magnetosphere boundary layer (the magnetopause) past the Moon. Velocity of the layer is determined by using arrival-time difference measurements at the two instruments along with known distances between the instruments along the direction of travel of the magnetopause.

lunar surface magnetometer and the lunar orbiting Explorer 35 magnetometer (fig. 43 shows an example of a magnetopause crossing). Assuming that the plane of a passing boundary layer is perpendicular to the solar ecliptic plane and that the boundary layer moves along its normal at the lunar orbit, the velocity of the layer is measured from arrival-time difference measurements and the known separation of the two magnetometers. In addition, the thickness of the bow shock and magnetopause are estimated by use of the calculated boundary speeds and the signature of the boundary in the magnetometer data. Measurements of the magnetospheric boundaries at the lunar orbit are pertinent to a complete understanding of the magnetic and plasma environment during each part of the Moon's orbit. Of particular current interest, is the interaction of the solar plasma with the moon as a particle-absorbing body (refs. 112 and 113), with the lunar ionsphere (refs. 114, 115, and 116), with the lunar remanent magnetic fields (refs. 25, 29, and 117), and with the induced lunar magnetosphere (refs. 51, 53, and 54).

To date, analysis has been carried out on seven evening and fifteen morning magnetopause crossings, and one evening and ten

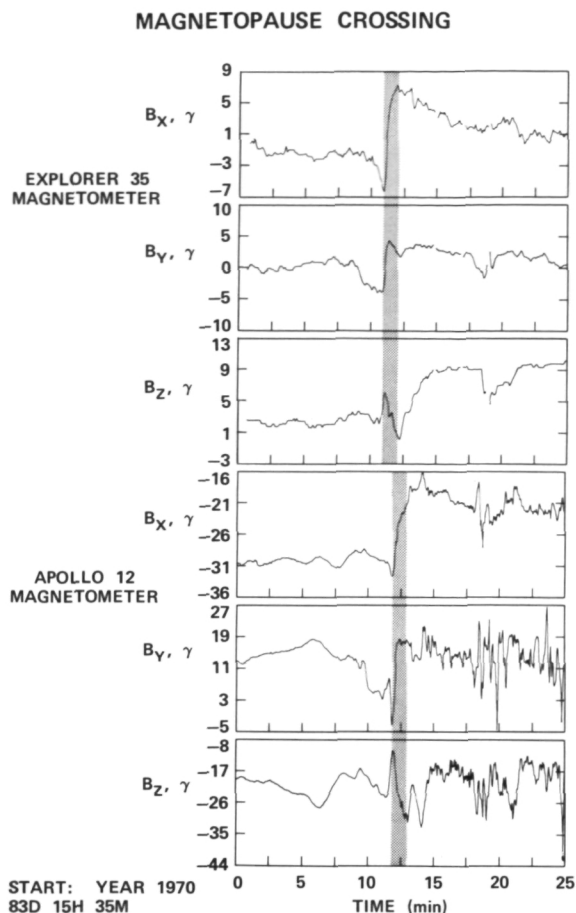


Figure 43.—Magnetopause crossing, measured by the Apollo 12 lunar surface magnetometer and the lunar orbiting Ames Explorer 35 magnetometer. Data are expressed in the lunar surface coordinate system which has its origin at the Apollo 12 magnetometer site;  $x$  is directed radially outward from the surface, while  $y$  and  $z$  are tangent to the surface, directed eastward and northward, respectively. Shaded regions show arrival times at the two instruments.

morning bow shock crossings (ref. 118). There appear to be no significant differences in the measured properties of the morning and evening boundaries at the lunar orbit, although statistics are limited. Elapsed-time data for shock and magnetopause motions, as measured by the magnetometers separated from each other by as much as  $10^4$  km, indicate that these boundaries are nearly always in motion and can have highly variable velocities. The magnetopause has an average

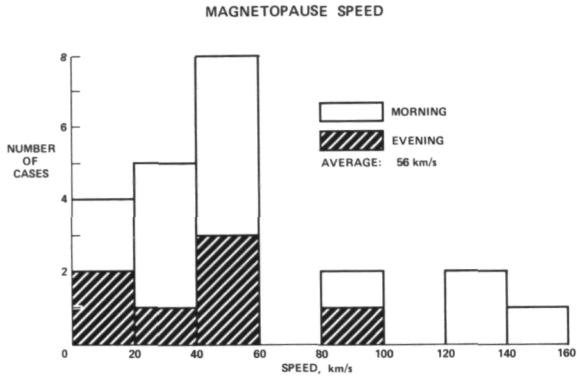


Figure 44.—Magnetopause speed distribution for 15 morning and 7 evening magnetopause crossings.

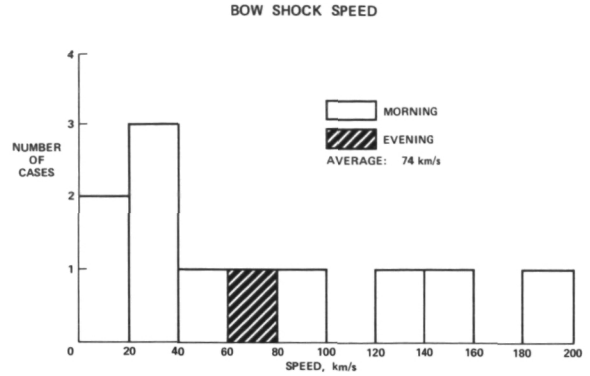


Figure 45.—Bow shock speed distribution for 1 evening and 10 morning bow shock crossings.

speed of about 50 kms/s but measurements vary from less than 10 km/s up to about 150 km/s (fig. 44). Similarly, the bow shock has an average speed of about 70 km/s but again there is a large spread in measured values from less than 10 km/s to about 200 km/s (fig. 45). The average measured magnetopause thickness is about 2300 km; however, individual magnetopause boundaries range from 500 km to 5000 km in thickness (fig. 46). The average bow shock thickness is determined to be about 1400 km, with a spread in individual values ranging from 220 km to 3000 km.

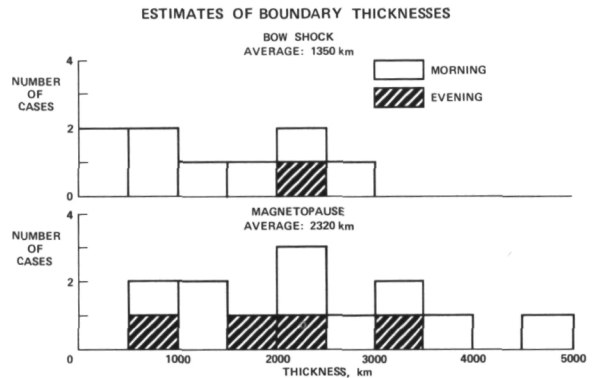


Figure 46.—Boundary thickness distributions calculated for 9 bow shock and 13 magnetopause crossings.

## Summary

### LUNAR REMANENT MAGNETIC FIELDS

Direct measurements of remanent fields have been made at nine sites on the lunar surface: 38  $\gamma$  at Apollo 12 in Oceanus Procellarum; 103  $\gamma$  and 43  $\gamma$  at two Apollo 14 sites separated by 1.1 km in Fra Mauro; 3  $\gamma$  at the Apollo 15 Hadley Rille site; and 189  $\gamma$ , 112  $\gamma$ , 327  $\gamma$ , 113  $\gamma$ , and 235  $\gamma$ , respectively at five Apollo 16 sites in the Descartes region, over a distance of 7.1 km. Simultaneous data from Apollo surface magnetometers and solar wind spectrometers show that the remanent fields at the Apollo 12 and 16 sites are compressed by the solar

wind. In response to a solar wind dynamic pressure increase of  $1.5 \times 10^{-7}$  dynes/cm<sup>2</sup>, the 38- $\gamma$  remanent field at the Apollo 12 LSM site is compressed to 54  $\gamma$ , whereas the field at the Apollo 16 LSM site correspondingly increases from 235  $\gamma$  to 265  $\gamma$ . Scale sizes of fields at the Apollo 12 and 16 sites are determined from properties of the remanent field-plasma interaction and orbiting magnetometer measurements. The Apollo 12 field scale size L is in the range  $2 \text{ km} \leq L \leq 200 \text{ km}$ , whereas for Apollo 16,  $5 \text{ km} \leq L \leq 100 \text{ km}$ .

Measurements by Apollo lunar magnetometers, and remanance in the returned samples, have yielded strong evidence that the lunar crustal material is magnetized over

much of the lunar globe. The surface measurements indicate that fields tend to be stronger in highland regions than in mare regions. The origin of lunar remanent fields remains an enigma. Possibilities are generally grouped under three classifications: a strong external (solar or terrestrial) field, an ancient intrinsic field of global scale, and smaller localized field sources.

### LUNAR MAGNETIC PERMEABILITY, INDUCED DIPOLE MOMENT, AND IRON ABUNDANCE

Simultaneous measurements by lunar magnetometers on the surface of the Moon and in orbit around the Moon are used to construct a whole-Moon hysteresis curve, from which the global lunar relative magnetic permeability is determined to be  $1.012 \pm 0.006$ . The global induced magnetization dipole moment corresponding to the permeability measurement is  $2 \times 10^{22} \text{H cm}^3$  (where H is magnetizing field in gauss). For typical geomagnetic tail fields of  $H \sim 10^{-4}$  gauss, the corresponding induced dipole moment is  $2 \times 10^{18}$  gauss-cm<sup>3</sup>. Both error limits on magnetic permeability value are greater than 1.0, implying that the Moon as a whole is paramagnetic and/or weakly ferromagnetic. Assuming that the ferromagnetic component is free metallic iron of multidomain, non-interacting grains, the free iron abundance in the Moon is calculated to be  $2.5 \pm 2.0$  wt.%. Total iron abundance in the moon is determined by combining free iron and paramagnetic iron components for two assumed lunar compositional models. For an orthopyroxene moon of overall density  $3.34 \text{ g/cm}^3$  with free iron dispersed uniformly throughout the lunar interior, the total iron abundance is  $12.8 \pm 1.0$  wt.%. For a free iron/olivine moon the total iron abundance is  $5.5 \pm 1.2$  wt.%. Iron abundance results are summarized in table 3 and figure 29.

Lunar models with a small iron core and with an iron-rich layer have been investigated by using the measured global lunar permeability as a constraint. A small pure iron core of 500-km radius (the maximum size

allowed by lunar density and moment of inertia measurements), which is hotter than the iron Curie point. ( $T > T_c$ ), would not be resolvable from the data since its magnetization field would be small compared with the measured induced field. Similarly, an iron-rich layer in the Moon could not be resolved if the iron is paramagnetic, i.e., if the iron is above the iron Curie temperature. Gast and Giuli (ref. 99) have proposed a family of high-density-layer models for the Moon which are geochemically feasible. If these models are iron-rich layers lying near the lunar surface so that  $T < T_c$ , the ferromagnetic layers would yield a global permeability value well above the measured upper limit. Therefore, it is concluded that such shallow iron-rich-layer models are not consistent with magnetic permeability measurements.

### LUNAR ELECTRICAL CONDUCTIVITY AND TEMPERATURE

The electrical conductivity of the lunar interior has been investigated by analyzing the induction of global lunar fields by time varying extralunar (solar or terrestrial) magnetic fields. An upper limit on the unipolar induction field has been determined which shows that at least the outer 5 km of the lunar crust is a relatively poor electrical conductor ( $< 10^{-9}$  mhos/m) compared with the underlying material. Past conductivity analyses have used magnetometer data recorded at times when global eddy-current fields were asymmetrically confined by the solar wind plasma. A time-dependent, transient-response analytical technique has been used in the studies. Transient analysis using lunar nightside data yields a conductivity profile rising from a range of values lying between  $1 \times 10^{-4}$  and  $2 \times 10^{-3}$  mhos/m at 250-km depth in the Moon to values ranging between  $2 \times 10^{-3}$  and  $8 \times 10^{-2}$  mhos/m at 1000-km depth. Transient analysis of day-side data yields a conductivity profile generally compatible with nightside transient results.

Recent conductivity analysis has considered

lunar eddy-current response during times when the moon is in the geomagnetic tail, in order to minimize the analytical problems posed by asymmetric solar wind confinement of the induced lunar magnetosphere. Preliminary results show that the following conductivity profile, though not unique, is compatible with input and response data: the conductivity increases rapidly with depth, from  $10^{-9}$  mhos/m at the surface to  $10^{-4}$  mhos/m at 200-km, then less rapidly to  $2 \times 10^{-2}$  mhos/m at 1000-km depth. By use of the conductivity-to-temperature relationship for olivine reported by Duba et al. (ref. 110), a temperature profile is calculated from this conductivity profile: temperature rises rapidly with depth to 1100 K at 200-km depth, then less rapidly to 1800 K at 1000-km depth.

## MAGNETOPAUSE AND BOW SHOCK PROPERTIES AT THE LUNAR ORBIT

Velocities and thicknesses of the Earth's magnetopause and bow shock at the lunar orbit have been estimated from simultaneous magnetometer measurements. Average speeds are about 50 km/s for the magnetopause and about 70 km/s for the bow shock, with large spreads in individual measured values. Average thicknesses are about 2300 km for the magnetopause and 1400 km for the bow shock, also with large spreads in individual measured values.

## References

1. COLBURN, D. S., R. G. CURRIE, J. D. MIHALOV, AND C. P. SONETT, Diamagnetic Solar-Wind Cavity Discovered Behind the Moon. *Science*, Vol. 158, 1967, p. 1040.
2. NESS, N. F., K. W. BEHANNON, C. S. SCEARCE, AND S. C. CANTARANO, Early Results From the Magnetic Field Experiment on Explorer 35. *J. Geophys. Res.*, Vol. 72, 1967, p. 5769.
3. MICHEL, F. C., Magnetic Field Structure Behind the Moon. *J. Geophys. Res.*, Vol. 73, 1968, p. 1533.
4. SPREITER, J. R., M. C. MARSH, AND A. L. SUMMERS, Hydromagnetic Aspects of Solar Wind Flow Past the Moon. *Cosmic Electrodynamics*, Vol. 1, 1970, p. 5.
5. SONETT, C. P., AND D. S. COLBURN, Establishment of a Lunar Unipolar Generator and Associated Shock and Wake by the Solar Wind. *Nature*, Vol. 216, 1967, p. 340.
6. SONETT, C. P., AND D. S. COLBURN, The Principle of Solar Wind Induced Planetary Dynamo. *Phys. Earth Planet. Interiors*, Vol. 1, 1968, pp. 326-346.
7. NESS, N. F., Electrical Conductivity of the Moon (abs.). *Trans. Am. Geophys. Union*, Vol. 49, 1968, p. 242.
8. BEHANNON, K. W., Intrinsic Magnetic Properties of the Lunar Body. *J. Geophys. Res.*, Vol. 73, 1968, p. 7257.
9. NESS, N. F., *Electrical Conductivity and Internal Temperature of the Moon*. Goddard Space Flight Center Report X-616-69-191, 1969. (Also presented as paper k 11 at COSPAR, Prague, May 1969.)
10. DOLGINOV, SH. SH., E. G. EROSHENKO, L. N. ZHUZGOV, AND N. V. PUSHKOV, Investigation of the Magnetic Field of the Moon. *Geomagnetics and Aeronomy*, Vol. 1, 1961, p. 18.
11. DOLGINOV, SH. SH., E. G. EROSHENKO, L. N. ZHUZGOV, AND N. V. PUSHKOV, Measurements of the Magnetic Field in the Vicinity of the Moon by the Artificial Satellite Luna 10. *Akad. Nauk USSR, Doklady*, Vol. 170, 1966, p. 574.
12. GOLD, T., The Magnetosphere of the Moon. In *The Solar Wind*, R. J. Mackin, Jr., and M. Neugebauer, eds., Pergamon Press, New York, 1966.
13. SONETT, C. P., D. S. COLBURN, AND R. G. CURRIE, The Intrinsic Magnetic Field of the Moon. *J. Geophys. Res.*, Vol. 72, 1967, p. 5503.
14. DEWYS, J. N., Results and Implications of Magnetic Experiments on Surveyor 5, 6, and 7 Spacecrafts (abs.). *Trans. Am. Geophys. Union*, Vol. 49, 1968, p. 249.
15. STRANGWAY, D. W., E. E. LARSON, AND G. W. PEARCE, Magnetic Studies of Lunar Samples—Breccia and Fines. *Proc. Apollo 11 Lunar Science Conference, Geochimica et Cosmochimica Acta*, Supplement 1, Vol. 3, A. A. Levinson, ed., 1970, p. 2435.
16. RUNCORN, S. K., D. W. COLLINSON, W. O'REILLY, M. H. BATTEY, A. A. STEPHENSON, J. M. JONES, A. J. MANSON, AND P. W. READMAN, Magnetic Properties of Apollo 11 Lunar Samples. *Proc. Apollo 11 Lunar Science Conference, Geochimica et Cosmochimica Acta*, Supplement 1, Vol. 3, A. A. Levinson, ed., 1970, p. 2369.
17. PEARCE, G. W., D. W. STRANGWAY, AND E. E. LARSON, Magnetism of Two Apollo 12 Igneous Rocks. *Proc. Second Lunar Science Conference, Geochimica et Cosmochimica Acta*, Supplement 2, Vol. 3, 1971, p. 2451.

18. NAGATA, T., R. M. FISHER, F. C. SCHWERER, M. D. FULLER, AND J. R. DUNN, Magnetic Properties and Remanent Magnetization of Apollo 12 Lunar Materials and Apollo 11 Lunar Microbreccia. *Proc. Second Lunar Science Conference, Geochimica et Cosmochimica Acta*, Supplement 2, Vol. 3, 1971, p. 2461.
19. NAGATA, T., R. M. FISHER, F. C. SCHWERER, M. D. FULLER, AND J. R. DUNN, Rock Magnetism of Apollo 14 and 15 Materials. *Proc. Third Lunar Science Conference, Geochimica et Cosmochimica Acta*, Supplement 3, Vol. 3, 1972, p. 2423.
20. COLLINSON, D. W., A. STEPHENSON, AND S. K. RUNCORN, Magnetic Properties of Apollo 15 and 16 Rocks. *Proc. Fourth Lunar Science Conference, Geochimica et Cosmochimica Acta*, Supplement 4, Vol. 3, 1973, p. 2963.
21. PEARCE, G. W., W. A. GOSE, AND D. W. STRANGWAY, Magnetic Studies on Apollo 15 and 16 Lunar Samples. *Proc. Fourth Lunar Science Conference, Geochimica et Cosmochimica Acta*, Supplement 4, Vol. 3, 1973, pp. 3045-3076.
22. GOSE, W. A., D. W. STRANGWAY, AND G. W. PEARCE, A Determination of the Intensity of the Ancient Lunar Magnetic Field. *The Moon*, Vol. 7, 1973, pp. 196-201.
23. DYAL, P., C. W. PARKIN, AND C. P. SONETT, Apollo 12 Magnetometer: Measurement of a Steady Magnetic Field on the Surface of the Moon. *Science*, Vol. 169, 1970, p. 726.
24. BARNES, A., P. CASSEN, J. D. MIHALOV, AND A. EVIATAR, Permanent Lunar Surface Magnetism and its Deflection of the Solar Wind. *Science*, Vol. 171, 1971, pp. 716-718.
25. MIHALOV, J. D., C. P. SONETT, J. H. BINSACK, AND MOUTSOULAS, Possible Fossil Lunar Magnetism Inferred From Satellite Data. *Science*, Vol. 171, 1971, p. 892.
26. COLEMAN, P. J., JR., B. R. LICHTENSTEIN, C. T. RUSSELL, L. R. SHARP, AND G. SCHUBERT, Magnetic Fields Near the Moon. *Proc. Third Lunar Science Conference, Geochimica et Cosmochimica Acta*, Supplement 3, Vol. 3, D. R. Criswell, ed., 1972, pp. 2271-2286.
27. SHARP, L. R., P. J. COLEMAN, JR., B. R. LICHTENSTEIN, AND C. T. RUSSELL, Orbital Mapping of the Lunar Magnetic Field. *The Moon*, Vol. 7, 1973, p. 322.
28. RUSSELL, C. T., P. J. COLEMAN, JR., B. R. LICHTENSTEIN, G. SCHUBERT, AND L. R. SHARP, Subsatellite Measurements of the Lunar Magnetic Field. *Proc. Fourth Lunar Science Conference, Geochimica et Cosmochimica Acta*, Supplement 4, Vol. 3, W. A. Gose, ed., 1973, pp. 2833-2845.
29. DYAL, P., C. W. PARKIN, C. W. SNYDER, AND D. R. CLAY, Measurements of Lunar Magnetic Field Interaction With the Solar Wind. *Nature*, Vol. 236, 1972, pp. 381-385.
30. CLAY, D. R., B. E. GOLDSTEIN, M. NEUGEBAUER, AND C. W. SNYDER, Solar-Wind Spectrometer Experiment. *Apollo 15 Preliminary Science Report*, NASA SP-289, 1972, pp. 10-1 to 10-7.
31. DYAL, P., AND C. W. PARKIN, The Magnetism of the Moon. *Sci. Amer.*, Vol. 225, 1971, pp. 62-73.
32. PARKIN, C. W., W. D. DAILY, AND P. DYAL, Iron Abundance in the Moon. *Proc. Fifth Lunar Science Conference, Geochimica et Cosmochimica Acta*, Vol. 3, 1974.
33. PARKIN, C. W., W. D. DAILY, AND P. DYAL, Lunar Iron Abundance From Magnetometer Measurements. *Lunar Science*, Vol. V, Part II, Lunar Science Institute, Houston, 1974, p. 589.
34. RUSSELL, C. T., P. J. COLEMAN, JR., B. R. LICHTENSTEIN, AND G. SCHUBERT, Permanent and Induced Magnetic Dipole Moment of the Moon. *Proc. Fifth Lunar Science Conference, Geochimica et Cosmochimica Acta*, Supplement 5, Vol. 3, W. A. Gose, ed., in press, 1974.
35. SCHWARTZ, K., AND G. SCHUBERT, Time-Dependent Lunar Electric and Magnetic Fields Induced by a Spatially Varying Interplanetary Magnetic Field. *J. Geophys. Res.*, Vol. 74, 1969, pp. 4777-4780.
36. SCHUBERT, G., AND K. SCHWARTZ, A Theory for the Interpretation of Lunar Surface Magnetometer Data. *The Moon*, Vol. 1, 1969, p. 106.
37. SILL, W. R., AND J. L. BLANK, Method for Estimating the Electrical Conductivity of the Lunar Interior. *J. Geophys. Res.*, Vol. 75, 1970, p. 201.
38. DYAL, P., AND C. W. PARKIN, The Apollo 12 Magnetometer Experiment: Internal Lunar Properties From Transient and Steady Magnetic Field Measurements. *Proc. Second Lunar Science Conference, Geochimica et Cosmochimica Acta*, Supplement 2, Vol. 3, 1971, p. 2391.
39. SMYTHE, W. R., *Static and Dynamic Electricity*. McGraw-Hill Book Co., New York, 1950.
40. WAIT, J. R., A Conducting Sphere in a Time Varying Magnetic Field. *Geophysics*, Vol. 16, 1951, p. 666.
41. TOZER, D. C., AND J. WILSON, The Electrical Conductivity of the Moon's Interior. *Proc. Roy. Soc. London*, Vol. A296, 1967, p. 320.
42. BLANK, J. L., AND W. R. SILL, Response of the Moon to the Time-Varying Interplanetary Magnetic Field. *J. Geophys. Res.*, Vol. 74, 1969, pp. 736-743.
43. DYAL, P., AND C. W. PARKIN, Electrical Conductivity and Temperature of the Lunar Interior From Magnetic Transient-Response

- Measurements. *J. Geophys. Res.*, Vol. 76, 1971, pp. 5947-5969.
44. SILL, W. R., Lunar Conductivity Models From the Apollo 12 Magnetometer Experiment. *The Moon*, Vol. 4, 1972, pp. 3-17.
  45. DYAL, P., C. W. PARKIN, AND W. D. DAILY, Surface Magnetometer Experiments: Internal Lunar Properties. *Proc. Fourth Lunar Science Conference, Geochimica et Cosmochimica Acta*, Supplement 4, Vol. 3, W. A. Gose, ed., 1973, pp. 2229-2945.
  46. SONETT, C. P., G. SCHUBERT, B. F. SMITH, K. SCHWARTZ, AND D. S. COLBURN, Lunar Electrical Conductivity From Apollo 12 Magnetometer Measurements: Compositional and Thermal Inferences. *Proc. Second Lunar Science Conference, Geochimica et Cosmochimica Acta*, Supplement 2, Vol. 3, 1971, pp. 2415-2431.
  47. SONETT, C. P., D. S. COLBURN, B. F. SMITH, G. SCHUBERT, AND K. SCHWARTZ, The Induced Magnetic Field of the Moon: Conductivity Profiles and Inferred Temperature. *Proc. Third Lunar Science Conference, Geochimica et Cosmochimica Acta*, Supplement 3, Vol. 3, 1972, p. 2309.
  48. KUCKES, A. F., Lunar Electrical Conductivity Profile. *Nature*, Vol. 232, 1971, p. 249.
  49. HOBBS, B. A., The Inverse Problem of the Moon's Electrical Conductivity. *Earth Planet. Sci. Letters*, Vol. 17, 1973, pp. 380-384.
  50. REISZ, A. C., D. L. PAUL, AND T. R. MADDEN, The Effects of Boundary Condition Asymmetries on the Interplanetary Magnetic Field-Moon Interaction. *The Moon*, Vol. 4, 1972, pp. 134-140.
  51. DYAL, P., AND C. W. PARKIN, Global Electromagnetic Induction in the Moon and Planets. *Phys. Earth Planet. Interiors*, Vol. 7, 1973, p. 251.
  52. SCHUBERT, G., K. SCHWARTZ, C. P. SONETT, D. S. COLBURN, AND B. F. SMITH, Lunar Electromagnetic Scattering II. Magnetic Fields and Transfer Functions for Parallel Propagation. *Proc. Fourth Lunar Science Conference, Geochimica et Cosmochimica Acta*, Supplement 4, Vol. 3, W. A. Gose, ed., 1973, pp. 2909-2923.
  53. SMITH, B. F., D. S. COLBURN, G. SCHUBERT, K. SCHWARTZ, AND C. P. SONETT, Induced Magnetosphere of the Moon 2. Experimental Results From Apollo 12 and Explorer 35. *J. Geophys. Res.*, Vol. 78, 1973, pp. 5437-5448.
  54. SCHUBERT, G., C. P. SONETT, K. SCHWARTZ, AND H. J. LEE, Induced Magnetosphere of the Moon I. Theory. *J. Geophys. Res.*, Vol. 78, 1973, pp. 2094-2110.
  55. DYAL, P., C. W. PARKIN, AND C. P. SONETT, Lunar Surface Magnetometer. *IEEE Trans. on Geoscience Electronics*, Vol. GE-8(4), 1970.
  56. GORDON, D. I., R. H. LUNDSTEN, AND R. A. CHIRADO, Factors Affecting the Sensitivity of Gamma-Level Ring-Core Magnetometers. *IEEE Trans. on Magnetics*, Vol. MAG-1(4), 1965, p. 330.
  57. GEYGER, W. A., *Nonlinear-Magnetic Control Devices*. McGraw-Hill Book Co., New York, 1964.
  58. SONETT, C. P., D. S. COLBURN, R. G. CURRIE, AND J. D. MIHALOV, The Geomagnetic Tail: Topology, Reconnection and Interaction With the Moon. In *Physics of the Magnetosphere*, R. L. Carovillano, J. F. McClay, and H. R. Radoski, eds., D. Reidel Publishing Co., Dordrecht, Holland, 1967.
  59. COLEMAN, P. J., JR., G. SCHUBERT, C. T. RUSSELL, AND L. R. SHARP, The Particles and Fields Subsatellite Magnetometer Experiment. *Apollo 15 Preliminary Science Report*, NASA SP-289, 1972, pp. 22-1 to 22-9.
  60. COLEMAN, P. J., JR., B. R. LICHTENSTEIN, C. T. RUSSELL, G. SCHUBERT, AND L. R. SHARP, The Particles and Fields Subsatellite Magnetometer Experiment. *Apollo 16 Preliminary Science Report*, NASA SP-315, 1972, pp. 23-1 to 23-13.
  61. MIHALOV, J. D., D. S. COLBURN, R. G. CURRIE, AND C. P. SONETT, Configuration and Reconnection of the Geomagnetic Tail. *J. Geophys. Res.*, Vol. 73, 1968, p. 943.
  62. HINNERS, N. W., The New Moon: A View. *Rev. Geophys. and Space Phys.*, Vol. 9, 1971, p. 447.
  63. NAGATA, T., R. M. FISHER, AND F. C. SCHWERER, Lunar Rock Magnetism. *The Moon*, Vol. 4, 1972.
  64. STRANGWAY, D. W., H. N. SHARP, W. A. GOSE, AND G. W. PEARCE, Magnetism and the Early History of the Moon. *Geochimica et Cosmochimica Acta*, Supplement 4, Vol. 37, in press, 1973.
  65. FULLER, M., Lunar Magnetism. *Rev. Geophys. and Space Sci.*, in press, 1974.
  66. SONETT, C. P., AND J. D. MIHALOV, Lunar Fossil Magnetism and Perturbations of the Solar Wind. *J. Geophys. Res.*, Vol. 77, 1972, p. 588.
  67. STRANGWAY, D. W., W. A. GOSE, G. W. PEARCE, AND R. K. MCCONNELL, Lunar Magnetic Anomalies and the Clayey Formation. *Nature*, Vol. 246, 1973, p. 112.
  68. WOOD, J. A., Thermal History and Early Magnetism in the Moon. *Icarus*, Vol. 16, 1972, pp. 229-240.
  69. STRANGWAY, D. W., AND H. A. SHARP, Lunar Magnetism and an Early Cold Moon. *Nature*, Vol. 249, 1974, p. 227.
  70. DYAL, P., C. W. PARKIN, C. P. SONETT, R. L. DUBOIS, AND G. SIMMONS, Lunar Portable Magnetometer Experiment. *Apollo 14 Preliminary Science Report*, NASA SP-272, 1971, pp. 227-237.

71. STRANGWAY, D. W., W. A. GOSE, G. W. PEARCE, AND J. G. CARNES, Magnetism and the History of the Moon. *Proc. 18th Annual Conference on Magnetism and Magnetic Material, J. Appl. Phys.*, in press, 1973.
72. DYAL, P., C. W. PARKIN, AND W. D. DAILY, Magnetism and the Interior of the Moon. Submitted to *Rev. Geophys. Space Phys.*, 1974.
73. SONETT, C. P., D. S. COLBURN, AND K. SCHWARTZ, Electrical Heating of Meteorite Parent Bodies and Planets by Dynamo Induction From Pre-main Sequence, T Tauri Solar Wind. *Nature*, Vol. 219, 1968, p. 924.
74. HELSLEY, C. E., Magnetic Properties of Lunar 10022, 10069, 10084, and 10085 Samples. *Proc. Apollo 11 Lunar Science Conference, Geochimica et Cosmochimica Acta*, Supplement 1, Vol. 3, 1970, p. 2213.
75. RUNCORN, S. K., D. W. COLLINSON, W. O'REILLY, A. STEPHENSON, M. H. BATTEY, A. J. MANSON, AND P. W. READMAN, Magnetic Properties of Apollo 12 Lunar Samples. *Proc. Roy. Soc. London, Ser. A*, Vol. 325, 1971, p. 157.
76. STRANGWAY, D. W., G. W. PEARCE, W. A. GOSE, AND R. W. TIMME, Remanent Magnetization of Lunar Samples. *Earth Planet. Sci. Letters*, Vol. 13, 1971, p. 43.
77. LEVY, E. H., Magnetic Dynamo in the Moon: A Comparison With Earth. *Science*, Vol. 178, 1972, p. 52.
78. UREY, H., AND S. K. RUNCORN, A New Theory of Lunar Magnetism. *Science*, Vol. 180, 1973, p. 636.
79. MURTHY, V. R., AND S. K. BANERJEE, Lunar Evolution: How Well Do We Know it Now. *The Moon*, Vol. 7, 1973, p. 149.
80. SMOLYCHOWSKI, R., Magnetism of the Moon. *The Moon*, Vol. 7, 1973, p. 127.
81. SCHUBERT, G., B. F. SMITH, C. P. SONETT, D. S. COLBURN, AND K. SCHWARTZ, Polarized Magnetic Field Fluctuations at the Site of Apollo 15: Possible Regional Influence on Lunar Induction. Submitted to *Science*, 1974.
82. NAGATA, T., Y. ISHIKAWA, H. KINOSHITA, M. KONO, Y. SYONO, AND R. M. FISHER, Magnetic Properties and Natural Remanent Magnetization of Lunar Materials. *Proc. Apollo 11 Lunar Science Conference, Geochimica et Cosmochimica Acta*, Supplement 1, Vol. 3, 1970, p. 2325.
83. CAP, F. F., Possible Production Mechanisms of Lunar Magnetic Fields. *J. Geophys. Res.*, Vol. 77, 1972, pp. 3328-3333.
84. DYAL, P., C. W. PARKIN, AND C. P. SONETT, Lunar Surface Magnetometer Experiment. *Apollo 12 Preliminary Science Report*, NASA SP-235, 1970, pp. 55-73.
85. PARKIN, C. W., P. DYAL, AND W. D. DAILY, Iron Abundance in the Moon From Magnetometer Measurements. *Proc. Fourth Lunar Science Conference, Geochimica et Cosmochimica Acta*, Supplement 4, Vol. 3, 1973, p. 2947.
86. ELLWOOD, W. B., A New Ballistic Galvanometer Operating in High Vacuum. *Rev. Sci. Inst.*, Vol. 5, 1934, pp. 300-305.
87. LINDEMAN, R., J. W. FREEMAN, JR., AND R. R. VONDRAK, Ions From the Lunar Atmosphere. *Proc. Fourth Lunar Science Conference, Geochimica et Cosmochimica Acta*, Supplement 4, Vol. 3, 1973, p. 2889.
88. UREY, H. C., *The Moon*. Z. Kopal and Z. K. Mikhailov, eds., Academic Press, 1962, p. 133.
89. REYNOLDS, R. T., AND A. L. SUMMERS, Calculations on the Composition of the Terrestrial Planets. *J. Geochim. Res.*, Vol. 74, 1969, p. 2494.
90. UREY, H. C., AND G. J. F. MACDONALD, Origin and History of the Moon. *Physics and Astronomy of the Moon*, Z. Kopal, ed., Academic Press, 1971, p. 213.
91. WÄNKE, H., H. BADDENHAUSEN, G. DREIBUS, M. QUIJANO-RICO, M. PALME, B. SPETTEL, AND F. TESCHKE, Multi-Element Analysis of Apollo 16 Samples and About the Composition of the Whole Moon. *Lunar Science*, Vol. IV, J. W. Chamberlain and C. Watkins, eds., Lunar Science Institute, Houston, 1973, pp. 761-763.
92. ZUSSMAN, J., The Mineralogy, Petrology and Geochemistry of Lunar Samples—A Review. *The Moon*, Vol. 5, 1972, p. 422.
93. WEEKS, R. A., Magnetic Phases in Lunar Material and Their Electron Magnetic Resonance Spectra: Apollo 14. *Proc. Third Lunar Science Conference, Geochimica et Cosmochimica Acta*, Supplement 3, Vol. 3, 1972, p. 2503.
94. UREY, H. C., K. MARTI, J. W. HANKINS, AND M. K. LIU, Model History of the Lunar Surface. *Proc. Second Lunar Science Conference, Geochimica et Cosmochimica Acta*, Supplement 2, Vol. 3, 1971, p. 987.
95. WOOD, J. A., J. S. DICKEY, U. B. MARVIN, AND B. J. POWELL, *Proc. Apollo 11 Lunar Science Conference, Geochimica et Cosmochimica Acta*, Supplement 1, Vol. 1, 1970, p. 965.
96. RINGWOOD, A. E., AND E. ESSENE, Petrogenesis of Lunar Basalts and the Internal Constitution and Origin of the Moon. *Science*, Vol. 167, 1970, pp. 607-610.
97. GREEN, D. H., A. E. RINGWOOD, N. G. WARE, W. O. HIBBERSON, A. MAJOR, AND E. KISS, Experimental Petrology and Petrogenesis of Apollo 12 Basalts. *Proc. Second Lunar Science Conference, Geochimica et Cosmochimica Acta*, Supplement 2, Vol. 1, A. A. Levinson, ed., 1971, pp. 601-615.

98. TOKSÖZ, M. N., Geophysical Data and the Interior of the Moon. *Ann. Rev. of Earth and Planet. Sci.*, Vol. 2, in press, 1973.
99. GAST, P. W., AND R. T. GIULI, Density of the Lunar Interior. *Earth Planet. Sci. Letters*, Vol. 16, 1972, p. 299.
100. DYAL, P., C. W. PARKIN, C. P. SONETT, AND D. S. COLBURN, *Electrical Conductivity and Temperature of the Lunar Interior From Magnetic Transient Response Measurements*. NASA TM X-62,012, 1970.
101. DYAL, P., C. W. PARKIN, AND W. D. DAILY, Temperature and Electrical Conductivity of the Lunar Interior From Magnetic Transient Measurements in the Geomagnetic Tail. *Proc. Fifth Lunar Science Conference, Geochimica et Cosmochimica Acta*, in press, 1974.
102. DYAL, P., C. W. PARKIN, AND P. CASSEN, Surface Magnetometer Experiments: Internal Lunar Properties and Lunar Surface Interactions With the Solar Plasma. *Proc. Third Lunar Science Conference, Geochimica et Cosmochimica Acta*, Supplement 3, Vol. 3, D. R. Criswell, ed., 1972, p. 2287.
103. SCHWARTZ, K., AND G. SCHUBERT, Lunar Electromagnetic Scattering, 1: Propagation Parallel to the Diamagnetic Cavity Axis. *J. Geophys. Res.*, Vol. 78, 1973, pp. 6496-6506.
104. PARKER, E. N., *Space Sci. Rev.*, Vol. 1, 1962, p. 62.
105. RIKITAKE, T., *Electromagnetism and the Earth's Interior*. Elsevier, Amsterdam, 1966.
106. ENGLAND, A. W., G. SIMMONS, AND D. STRANGWAY, Electrical Conductivity of the Moon. *J. Geophys. Res.*, Vol. 73, 1968, p. 3219.
107. DUBA, A., H. C. HEARD, AND R. N. SCHOCK, The Lunar Temperature Profile. *Earth Planet. Sci. Letters*, Vol. 15, 1972, p. 301.
108. DUBA, A., Electrical Conductivity of Olivine. *J. Geophys. Res.*, Vol. 77, 1972, p. 2483.
109. DUBA, A., AND A. E. RINGWOOD, Electrical Conductivity, Internal Temperatures and Thermal Evolution of the Moon. *The Moon*, Vol. 7, 1973, p. 356.
110. DUBA, A., H. C. HEARD, AND R. N. SCHOCK, Electrical Conductivity of Olivine at High Pressure and Under Controlled Oxygen Fugacity. *J. Geophys. Res.*, Vol. 79, 1974, p. 1667.
111. DUBA, A., AND I. A. NICHOLLS, The Influence of Oxidation State on the Electrical Conductivity of Olivine. *Earth Planet. Sci. Letters*, Vol. 18, 1973, pp. 59-64.
112. ANDERSON, K. A., L. M. CHASE, R. P. LIN, J. E. MCCOY, AND R. E. MCGUIRE, Solar-Wind and Interplanetary Electron Measurements on the Apollo 15 Subsatellite. *J. Geophys. Res.*, Vol. 77, 1972, pp. 4611-4626.
113. GEISS, J., F. BUHLER, H. CERUTTI, AND P. EBERHARDT, Solar Wind Composition Experiment. *Apollo 15 Preliminary Science Report*, NASA SP-289, 1972, pp. 15-1 to 15-7.
114. CRISWELL, D. R., Photoelectrons and Solar Wind/Lunar Limb Interaction. *The Moon*, Vol. 7, 1973, p. 202.
115. MANKA, R. H., AND F. C. MICHEL, Lunar Ion Energy Spectra and Surface Potential. *Proc. Fourth Lunar Science Conference, Geochimica et Cosmochimica Acta*, Supplement 4, Vol. 3, W. A. Gose, ed., 1973, pp. 2897-2908.
116. RICH, F. J., D. L. REASONER, AND W. J. BURKE, Plasma Sheet at Lunar Distance: Characteristics and Interactions With the Lunar Surface. *J. Geophys. Res.*, Vol. 78, 1973, pp. 8097-8112.
117. NEUGEBAUER, M., C. W. SNYDER, D. R. CLAY, AND B. E. GOLDSTEIN, Solar Wind Observations on the Lunar Surface With the Apollo 12 ALSEP. *Planetary and Space Sci.*, Vol. 20, 1972, pp. 1577-1591.
118. DAILY, W. D., P. DYAL, AND C. W. PARKIN, Magnetopause Velocity and Thickness From a Network of Apollo Magnetometers (abs.). *Trans. Amer. Geophys. Union (EOS)*, Vol. 55, 1974, p. 390.
119. HANKS, T. C., AND D. L. ANDERSON, Origin, Evolution, and Present Thermal State of the Moon. *Phys. Earth Planet. Interiors*, Vol. 5, 1972, pp. 409-425.